

Return of 4U 1730–22 after 49 years silence: the outburst properties observed by NICER and Insight-HXMT

Yu-Peng Chen^{*}

chenyp@ihep.ac.cn

Key Laboratory for Particle Astrophysics, Institute of High Energy Physics, Chinese Academy of Sciences, 19B Yuquan Road, Beijing 100049, China

Shu Zhang^{*}

szhang@ihep.ac.cn

Key Laboratory for Particle Astrophysics, Institute of High Energy Physics, Chinese Academy of Sciences, 19B Yuquan Road, Beijing 100049, China

Shuang-Nan Zhang^{*}

zhangsn@ihep.ac.cn

Key Laboratory for Particle Astrophysics, Institute of High Energy Physics, Chinese Academy of Sciences, 19B Yuquan Road, Beijing 100049, China
University of Chinese Academy of Sciences, Chinese Academy of Sciences, Beijing 100049, China

Long Ji

School of Physics and Astronomy, Sun Yat-Sen University, Zhuhai, 519082, China

Peng-Ju Wang

Key Laboratory for Particle Astrophysics, Institute of High Energy Physics, Chinese Academy of Sciences, 19B Yuquan Road, Beijing 100049, China
University of Chinese Academy of Sciences, Chinese Academy of Sciences, Beijing 100049, China

Ling-Da Kong

Institut für Astronomie und Astrophysik, Kepler Center for Astro and Particle Physics,
Eberhard Karls Universität, Sand 1, D-72076 Tübingen, Germany

Zhi Chang

Key Laboratory for Particle Astrophysics, Institute of High Energy Physics, Chinese
Academy of Sciences, 19B Yuquan Road, Beijing 100049, China

Jing-Qiang Peng

Key Laboratory for Particle Astrophysics, Institute of High Energy Physics, Chinese
Academy of Sciences, 19B Yuquan Road, Beijing 100049, China
University of Chinese Academy of Sciences, Chinese Academy of Sciences, Beijing 100049,
China

Qing-Cang Shui

Key Laboratory for Particle Astrophysics, Institute of High Energy Physics, Chinese
Academy of Sciences, 19B Yuquan Road, Beijing 100049, China
University of Chinese Academy of Sciences, Chinese Academy of Sciences, Beijing 100049,
China

Jian Li

CAS Key Laboratory for Research in Galaxies and Cosmology, Department of Astronomy,
University of Science and Technology of China, Hefei 230026, China
School of Astronomy and Space Science, University of Science and Technology of China,
Hefei 230026, China

Lian Tao

Key Laboratory for Particle Astrophysics, Institute of High Energy Physics, Chinese
Academy of Sciences, 19B Yuquan Road, Beijing 100049, China

Ming-Yu Ge

Key Laboratory for Particle Astrophysics, Institute of High Energy Physics, Chinese
Academy of Sciences, 19B Yuquan Road, Beijing 100049, China

Jin-Lu Qu

Key Laboratory for Particle Astrophysics, Institute of High Energy Physics, Chinese
Academy of Sciences, 19B Yuquan Road, Beijing 100049, China

Received _____; accepted _____

ABSTRACT

After in quiescence for 49 years, 4U 1730–22 became active and had two outbursts in 2021 & 2022, the onset and tail of the outbursts were observed by NICER, which give us a peerless opportunity to study the state transition and its underlying mechanism. In this work, we take both the NS surface and accretion disk emission as the seed photons of the Comptonization and derive their spectral evolution in a bolometric luminosity range of 1%–15% L_{Edd} . In the high/soft state, the inferred inner disk radius and the NS radius are consistent well, which implies that the accretion disk is close to the NS surface. For the decay stage, we report a steep change of the accretion disk emission within one day, i.e., the soft-to-hard transition, which could be due to the propeller effect and the corresponding neutron star surface magnetic field is $1.8\text{--}2.2 \times 10^8$ G. Moreover, the inner disk radius is truncated at the corotation radius, which is similar to the propeller effect detected from 4U 1608–52. The absence of the propeller effect in the hard-to-soft state transition implies that the transition between the magnetospheric accretion and the disk accretion is not the sole cause of the state transitions.

Subject headings: stars: coronae — stars: neutron — X-rays: individual (4U 1730–22)
— X-rays: binaries — X-rays: outbursts

1. Introduction

About one third of low mass X-ray binaries (LMXBs) hosting neutron stars (NS) are transient sources and characterized by a luminosity that varies over $\sim 10^{32} - 10^{38} \text{ erg}^{-2}\text{s}^{-1}$, which is likely caused by an instability of the accretion induced by a variable accretion rate, \dot{M} . In this picture, the accretion flow drained from the companion star propagates towards the NS from the outer regions of the accretion disk (see review, e.g., Done et al. 2007), which is confirmed by multi-wavelength observations (e.g., López-Navas et al. 2020). Except for the accretion rate, the NS’s parameters, e.g., magnetic field and spin period, could also affect the accretion process. In theory, the luminosity’s abrupt drop at $\sim 10^{36} - 10^{37} \text{ erg}^{-2} \text{ s}^{-1}$ in NS-LMXBs is produced by a transition from the disk accretion (material drops onto the NS surface) to the magnetospheric accretion (material drops on the magnetosphere and is then expelled out from the system), i.e., the propeller effect (Zhang et al. 1998). **The interaction between the magnetic field and the accretion disk occurs in many types of stars involving young stellar objects, white dwarfs, and NSs, which has influence on the inner disk radius, outflow rate and etc (e.g., Ustyugova et al. 2006; Romanova & Owocki 2015; Bozzo et al. 2009; Campana et al. 2018).**

In this picture, the propeller effect happens when the accretion rate is low enough that the magnetospheric radius, r_m (at which the ram pressure of the infalling material is balanced against the magnetic pressure) is larger than the corotation radius r_c (at which gravitational forces and centrifugal forces are balanced) (Illarionov & Sunyaev 1975; Cui 1997),

$$r_c = 1.7 \times 10^8 P_{\text{spin}}^{2/3} M_{1.4}^{1/3} \text{ cm}, \quad (1)$$

here P is the NS spin period in units of second, $M_{1.4}$ is the NS mass in units of $1.4M_{\odot}$. That is, if $r_m > r_c$ the accretion disk is truncated at r_m and the accreted material is

mostly “propelled” out by the spinning magnetosphere, rather than falling down to the NS surface. The transition causes a luminosity gap (Corbet 1996; Campana & Stella 2000), $\Delta \equiv r_m/r_{\text{NS}} \geq r_c/r_{\text{NS}}$. This gap has a lower limit value, r_c/r_{NS} , which is only dependent on the NS mass M_{NS} , NS radius r_{NS} , and NS spin P_{spin} .

4U 1730–22 was detected by Uhuru in 1972 (Cominsky et al. 1978; Forman et al. 1978), and after half a century of quiescence it returned to be active in 2021 and 2022. The bright luminosity in the quiescent state (Tomsick et al. 2007), thermonuclear bursts (type I X-ray bursts) (Chen et al. 2022b; Li et al. 2022), and the burst oscillation around $\nu=584.65$ Hz (Li et al. 2022), indicate its NS nature and its magnetic field $\sim 10^8 - 10^9$ G. NICER and Insight-HXMT made high cadence observations on the two outbursts and covered the whole outburst stage: the onset, the peak, and the extinction, which is an ideal sample to study the accretion process, e.g., the ‘propeller effect’ and the luminosity gap during the state transition. For 4U 1730–22, $r_c=24$ km, and it is predicted $\Delta = 2.4$ by assuming $M_{\text{NS}}=1.4 M_{\odot}$, $r_{\text{NS}}=10$ km.

In this work, using the broad energy band capabilities of Insight-HXMT and the large effective area in soft X-ray band of NICER, we study the two outbursts from 4U 1730–22. In previous works, when the outburst spectrum is fitted, the accretion disk emission is usually taken as seed photon component and the NS surface emission is ignored, or the NS surface emission is taken as the seed photon component but the accretion disk emission is ignored, e.g., (Zhang et al. 1998; Chen et al. 2006). This is due to that the faint NS surface emission of less than one-tenth of the disk emission when the source is bright or that it is hard to distinguish them due to the constraints of the previous instruments. However, when the accretion rate is very low, i.e., $\sim 1\%L_{\text{Edd}}$, the NS surface emission could not be ignored, and should be involved in the spectral fitting. Especially, in the onset and the extinction of the outburst, the NS surface is the main seed photon component and is

much brighter than the disk emission. In this work, by stacking observations when the source is very faint, the disk emission and the NS surface emission are both involved in the spectral fitting, and the disk radius and temperature are obtained (Section 2 and Section 3). Moreover, a state transition with a luminosity’s abrupt drop is observed by NICER, which could be caused by the propeller effect (Section 4).

2. Observations and Data Reduction

2.1. Insight-HXMT

Insight-HXMT was launched on the 15th of June 2017, which excels in its broad energy band (1–250 keV), large effective area in the hard X-rays energy band and little pile-up for bright sources (up to several Crab) (Zhang et al. 2020). There are three main payloads, and all of them are collimated telescopes: the High Energy X-ray Telescope (HE; poshwich NaI/CsI, 20–250 keV, $\sim 5000 \text{ cm}^2$), the Medium Energy X-ray Telescope (ME; Si pin detector, 5–40 keV, 952 cm^2) and the Low Energy X-ray telescope (LE; SCD detector, 1–12 keV, 384 cm^2). For the three main payloads of Insight-HXMT, each has two main field of views (FoVs), i.e., LE: $1.6^\circ \times 6^\circ$ and $6^\circ \times 6^\circ$, ME: $1^\circ \times 4^\circ$ and $4^\circ \times 4^\circ$, HE: $5.7^\circ \times 1.1^\circ$ and $5.7^\circ \times 5.7^\circ$. Moreover, they also have the blind FoV (full blocked) detectors, which are used for the background estimation and energy calibration.

As shown in Figure 1, for the two outbursts in 2021 and 2022, Insight-HXMT observed 4U 1730–22 with 74 observations ranging from P041401100101-20210707-01-01 to P051400201402-20220513-02-01 with a total observation time of 184 ks. These observations covered the peak and decay phases of the outburst in 2021 and the peak stage of the outburst in 2022. The HE spectrum is not involved in the joint spectral fitting of the persistent emission, since the expected HE flux falls below the systematic error of the

background model.

We use the Insight-HXMT Data Analysis software (HXMTDAS) v2.05¹ to extract the lightcurves, the spectra and background emission following the recommended procedure of the Insight-HXMT Data Reduction. For the spectral fitting of LE and ME, the energy bands are chosen to be 2–7 keV and 8–20 keV. The spectra of LE and ME are rebinned by ftool ftgrouppha optimal binning algorithm (Kaastra & Bleeker 2016) with a minimum of 25 counts per grouped bin, and a 1% systematic error is added to account for the uncertainties of the background model and calibration (Li et al. 2020). The resulting spectra are analyzed using XSPEC (Arnaud 1996) version 12.12.0.

2.2. NICER

For the two outbursts, NICER also performed high cadence observations, which covered almost all the stages of the two outbursts but missed the onset and rise stage of the outburst in 2022. NICER has observed 4U 1730–22 with 162 observations ranging from 4202200101 to 4639010210 with a total exposure time of 372 ks.

The NICER data are reduced using the pipeline tool nicerl2² in NICERDAS v7a with the standard NICER filtering and using ftool XSELECT to extract lightcurves and spectra. Among the 52 operational detectors, the Focal Plane Module (FPM) No. 14 and 34 are removed from the analysis because of increased detector noise. The response matrix files (RMFs) and ancillary response files (ARFs) are generated with the ftool nicerrmf and nicerarf. The background is estimated using the ftool nibackgen3C50 (Remillard et al. 2022). As we did for the Insight-HXMT spectra, the spectra of NICER are rebinned by

¹<http://hxmtweb.ihep.ac.cn/>

²https://heasarc.gsfc.nasa.gov/docs/nicer/nicer_analysis.html

ftool ftgrouppha optimal binning algorithm (Kaastra & Bleeker 2016) with a minimum of 25 counts per grouped bin.

The tbabs model with Wilm abundances accounts for the ISM absorption in the spectral model (Wilms et al. 2000). We added a systematic uncertainty of 1% to the NICER spectrum in 1–10 keV and 5% to the NICER spectrum in 0.4–1 keV because of a larger systematic uncertainty caused by the NICER instrument and the unmodelled background.

A color-color diagram (CCD) is attempted to plot from NICER data or MAXI data, however, the trajectory in the plot is not a coherent way to represent systems, which could be due to the narrow energy band of NICER and low sensitivity of MAXI. Thus we plot a hardness-intensity diagram (HID), as shown in Figure 2, where ‘hardness’ is defined as the count rate ratio (2.5–10 keV/1.7–2.5 keV) and ‘intensity’ is defined the count rate in 0.4–10 keV. Each point on HID represents an obsid with an exposure time of ~ 1000 –5000 s. The black points and red points represent the outbursts in 2021 and 2022, respectively.

3. Analysis and Results

The obsids with thermonuclear bursts observed both by NICER and Insight-HXMT have been removed from the data before attempting spectral fits of the observations, since the additional thermal photons could alter the spectral fitting results of the persistent emission. These obsids all located at the peak phase of the outbursts, it does not affect the spectral evolution of the outbursts when these obsids are removed. Moreover, some obsids with sharp variations in the lightcurves caused by the incorrect good-time-interval are also removed. For the outburst onset of 2021 and extinction time of the outburst

in 2022, i.e., the lowest count rates obsids (~ 30 cts/s) in Figure 2, the spectra of several obsids are stacked by the ftool `addspec`, respectively. We fit the two stacked spectra with an absorbed convolution thermal Comptonization model (with input photons contributed by the spectral component blackbody, i.e., `tbabs*thcomp*bb`), available as `thcomp` (a more accurate version of `nthcomp`) (Zdziarski et al. 2020) in XSPEC, which is described by the optical depth τ , electron temperature kT_e , scattered/covering fraction f_{sc} . The hydrogen column (`tbabs` in XSPEC) accounts for both the line-of-sight column density and any intrinsic absorption near the source. The seed photons are in the shape of blackbody since the `thcomp` model is a convolution model, and a fraction of Comptonization photons are also given in the model. The results of the spectral fitting are presented in Table 1 and plotted in Figure 3 and Figure 4. The inferred blackbody radius is well consistent with the NS radius under a distance of 7.56 kpc (Li et al 2022), thus a spherical corona scenario is favored since the scattered/covering fraction $f_{sc} > 70\%$ at this stage. We also notice that the blackbody temperature of the two stacked spectra are both around 0.45 keV and the bolometric fluxes of them are also very similar.

Along with the increase of the count rates, the model above is also attempted to fit the obsids with count rate > 40 . However, the parameters derived from the above model is unreasonable, e.g., the blackbody radius R_{bb} is much larger than 10 km and up to more than 100 km, which is much larger than the NS radius. Moreover, the blackbody temperature kT_{bb} decreases as the count rate increases, which is also very unlikely. For the obsids in the rising phase of the outburst in 2021 with luminosity ($4.5\text{--}13.8 \times 10^{-9}$ erg/cm²/s) and count rate (70–190 cts/s) which are similar to that of the two obsid of the soft-to-hard state transition (see the next paragraph), the inferred kT_{bb} is 0.39–0.11 keV and 20–120 km. Under this condition, the spherical corona scenario is disfavored during the rising phase of the outburst. Thus, we assume the NS surface emission (the temperature and the area) does not change during the outbursts, and take it

as part of the seed photons of the Comptonization, **i.e., $\text{tbabs}*\text{thcomp}*(\text{bb}+\text{diskbb})$ with the fixed blackbody parameters derived from the spectral fitting at the outburst onset.** This assumption should underestimate the NS surface emission and thus leads to an overestimate the accretion disk emission/radius, since kT_{bb} should be higher as the accretion rate increases. The underestimation of the inclination angle (we take $\theta = 0$ to calculate the inner disk radius) could offset the overestimation above of the disk emission/radius. Some works (Thompson et al, 2005; Zand et al. 2009) indicated that the NS surface temperature could be up to 0.6–0.8 keV and partial of the NS surface emission is blocked by the disk (Thompson et al, 2005) and not involved in the Comptonization, which could also offset the overestimate the accretion disk emission/radius. As given in the following paragraph, the derived inner radii are consistent well with the NS radius, which indicates this assumption has a mild influence on the spectral fitting and is accepted.

For consistency check, we also fit the spectra by removing the NS surface emission, the derived model parameters are shown in the Appendix both for the tables and figure. For obsids around the peak of the outbursts (e.g., with count rates > 200 cts/s), it has an insignificant influence on the derived parameters of the thcomp and diskbb , since the flux of the disk is more than ten times higher than the blackbody emission. However, for the obsids around the rising and decaying parts of the outburst (e.g., with count rates < 100 cts/s), the influence is significant since the flux of the disk is comparable with the blackbody emission; e.g. for the obsids 4639010182–4639010187 around the propeller effect, the derived T_{disk} changes from 0.6 to 1.0 keV and R_{disk} changes from 10 to 2 km, which is unlikely because of the non-physical temperature trend and the small inner disk radius. Moreover, the model of the spherical corona scenario ($\text{tbabs}*\text{thcomp}*\text{bb}$) is also attempted to fit obsids 4639010182–4639010187 around this transition, and the derived T_{bb} changes

from 0.35 keV to 0.48 keV and R_{bb} changes from 45 km to 16 km, which is also unlikely because of the non-physical trend of the temperature and the large NS radius. After the transition, e.g., the obsids 4639010188–4639010196 with count rates $\sim 52\text{--}40$ cts/s, the derived T_{bb} changes from 0.40 keV to 0.35 keV and R_{bb} changes from 16 km to 11 km in the spherical corona scenario, which indicates that the data quality of these obsids could not identify whether the spherical corona or the disk corona scenario is more reasonable. Given the overall consistency and reasonable evolution of model parameters of the model including both components of the NS surface and accretion disk emission, we take this model as physically more appropriate than that with only one thermal emission component.

We then take the thermal emission from the accretion disk as the other part of the seed photons to fit the obsids with count rates > 40 cts/s, i.e., the model is revised to `tbabs*thcomp*(bb+diskbb)` with the fixed blackbody parameters derived from the spectral fitting at the outburst onset. From the revised model, the derived parameters are reasonable, as shown in Table 3, Figure 3 and Figure 5. **Please note that the error bars of the disk temperature T_{disk} , inner disk radii R_{disk} and the bolometric fluxes F of some obsids (mostly with counts rates < 60 ct/s) with $T_{\text{disk}} \sim 0.1\text{--}0.2$ keV is hard to be derived because of the low temperature and low flux of the disk emission, and we fixed other parameters to calculate T_{disk} , R_{disk} , and F , which should underestimate these error bars. We also attempt to stack several of them, and the derived parameters are consistent with that derived from the individual obsid.** The model is also used to fit the joint spectra of NICER and Insight-HXMT, as shown in Table 2 and Figure 3. Under a distance of 7.56 kpc, and $L_{\text{Edd}} = 1.8 \times 10^{38}$ erg/s, the peak luminosity corresponds to $\sim 15\%$ L_{Edd} . Along with the increased flux, at the rising phase of the outburst, the inner disk radius

R_{disk} is above 20 km, and then stays at ~ 10 km after the flux peak time in the face-on scenario (inclination angel $\theta = 0$). At the decay phase of the outburst in 2022, an abrupt change of R_{disk} and T_{disk} between obsids 4639010184 and 4639010185 is obvious, i.e., from 0.5 keV and 12 km to 0.3 keV and 24 km within one day. NICER missed the decay phase of the outburst in 2021 with a gap about 40 days. Please note that there are some differences of the thcomp parameters derived from the joint NICER/Insight-HXMT spectral fitting and the NICER spectral fitting, but the trends are very similar. It is because that the shape of the unsaturated Comptonization is more dependant on the higher energy photons which undergo more scatterings than the mean or the lower energy photons. The joint spectral fitting extends the photon energy from 10 keV to 20 keV, and the derived thcomp parameters should be more reliable. We also notice that the disk parameters derived from the two kinds of spectra are consistent well with each other.

Moreover, the enlarged R_{disk} is consistent well with the corotation radius r_c , both of which are around 24 km. The transition is also obvious in the HID, as shown in Figure 2, with count rates from 174 cts/s to 85 cts/s within one day. We also notice that, different from the bolometric luminosity of the disk F_{disk} which decreases by a factor of 2.9 during the transition, however, the parameters of the Comptonization model changed little. This leads to that the total bolometric luminosity shows a mild change by a factor of 1.6.

Under a distance of 7.56 kpc, the transition occurred is between obsids 4639010184 and 4639010185 in Table 3, with the bolometric luminosities of 5.4×10^{36} erg s $^{-1}$ and 3.4×10^{36} erg s $^{-1}$, respectively. Assuming $M_{\text{NS}} = 1.4 M_{\odot}$, $R_{\text{NS}} = 10$ km, and taking $P_{\text{spin}} = 1/587 = 1.71$ ms, the inferred magnetic fields corresponding to the two luminosities above are 1.8×10^8 G and 2.2×10^8 G, respectively, based on the formula given by Lamb et al. (1973); Cui (1997); Zhang et al. (1998)

$$L_{X,36} \approx 2.34 B_9^2 P_{-2}^{-7/3} M_{1.4}^{-2/3} R_6^5, \quad (2)$$

here $L_{X,36}$ is the total luminosity in units of 10^{36} erg s $^{-1}$, B_9 is the magnetic field in units of 10^9 G, P_{-2} is the NS period in units of 10 ms, $M_{1.4}$ is the NS mass in units of $1.4M_\odot$ and R_6 is the NS radius in units of 10 km.

4. Discussion

Different from the previous work on the propeller effect, we take both the NS surface and accretion disk emission as the seed photons of the Comptonization and get the time evolution of the corona and disk in the bolometric luminosity range of 1%–15% L_{Edd} . The HID shows a hysteresis, i.e., the luminosity of the hard-to-soft transition is higher than the luminosity of the soft-to-hard transition. However, the first transition above (hard-to-soft) was not observed by NICER due to its observation gap. Fortunately, the last transition above (soft-to-hard) was detected by NICER and shows a sudden decline in accretion disk emission. The truncated inner disk radius is consistent well with the corotation radius. Taking the soft-to-hard transition as caused by the propeller effect, the magnetic field is derived. Apart from Aql X-1 (Zhang et al. 1998) and 4U 1608-52 (Chen et al. 2006), 4U 1730-22 is now also listed among the sources with observed propeller effect.

We notice that the total luminosity change during the transition is by a factor of 1.6, which is smaller than the model-predicted luminosity gap of 2.4, and could be related to matter leaking through the magnetosphere to the NS surface (e.g., Stella, White & Rosner 1986; Zhang et al. 1998), e.g., forming some kind of accretion flow/channel to the NS surface (e.g., magnetic poles) (Arons & Lea 1976; Elsner & Lamb 1977), as shown in Figure 6. If it were true, a reasonable prediction is that there is an enhancement of pulsation fraction (if the pulsation exists) around the transition, which is beyond scope of this work and will be explored elsewhere.

For the outbursts of 4U 1730–22, the picture aforementioned in Section 1 is revised as shown in the toy model of Figure 6. In the high/soft state, the accretion disk extends to the NS surface. Along with the accretion rate to a certain value, the propeller effect happens and expels out most material within the magnetosphere, which leads to a truncated disk (at the corotation radius for this work). However, there is still partial material that could be leaked to the NS surface. At end of the outburst, the inner radius of the accretion disk and the radius of the magnetosphere is far from the NS, i.e., the spherical corona scenario.

Particularly, we notice that the two luminosities above are roughly the same as the transition luminosities detected by RXTE in 2004 from 4U 1608–52 (Chen et al. 2006), e.g., 5.3×10^{36} erg s^{−1} and 3.3×10^{36} erg s^{−1}. Considering that the spin periods of the two systems are similar, e.g., the spin period of 4U 1608–52 is 1.16 ms, the behavior of the outburst should resemble each other. The similar outburst’s behavior is reminiscent of the similar thermonuclear bursts’ (type I X-ray bursts) behavior of the two systems (Chen et al. 2022a,b), e.g., the bright photospheric radius expansion (PRE) bursts show a shortage during the rising PRE phase which could be due to the occlusion by the disk which is close to the NS surface during their high/soft state.

Moreover, the luminosity gap ratio of ‘2.4’ works only at the aligned case, i.e., aligned magnetic and spin axes, which are both perpendicular to the plane of the disk; a large inclination angle between the NS rotation and magnetic field axes leads to a smaller gap ratio, from a mechanism that has been supported by theory and simulations several works (e.g., Bozzo et al. 2009; Romanova & Owocki 2015; Bozzo et al. 2018). In this quasi-magnetospheric accretion scenario, if the matter accumulates around the magnetospheric radius faster than it can be ejected, the episodic or cyclic outbursts could occur (D’Angelo & Spruit 2012; Lii et al. 2014). We notice that after this work,

4U 1730–22 started a new outburst in September and October 2022, which implies this source stepped into an active phase and could be related the mass accumulation mentioned above.

Both for black hole (BH)-LMXBs and NS-LMXBs, around the soft-to-hard state transition, the luminosity shows a fast decay stage, which is the ‘knee’ feature (Powell et al. 2007). For the NS-LMXBs, it could be related to the propeller effect. However, for BH-LMXBs, the propeller effect is not expected in absence of magnetic field, another scenario—the thermal disk instability could be related to the ‘knee’ feature, which could be also related to the hard-to-soft transition (Maccarone & Coppi 2003). In the rising phase of the outburst in 2021 from 4U 1730–22, we notice that at the same luminosity of the soft-to-hard state transition, the transition of the hard-to-soft state did not happen, but could have occurred at a higher luminosity and not observed due to the observation gap, i.e., the hysteresis (Fender & Belloni 2004). Maccarone & Coppi (2003) proposed that the transitions between the optically thick and optically thin corona are related to the hard-to-soft and soft-to-hard transitions, and thus the propeller effect is not the sole cause of the state transitions.

The above calculation and estimation are based on the static analysis and do not consider the radial velocity component of the innermost accretion disk, i.e., the inertia of the disk. In the rising phase of the outburst, the accretion disk has a radial velocity towards the NS and the inflow is easier to overcome the magnetic stress; in contrast, in the decay phase the accretion disk has a radial velocity outwards from the NS and the inflow is harder to overcome the magnetic stress. In other words, the higher inflow rate of the rising phase could fill the luminosity gap caused by the propeller factor more significantly than that of the decay phase. The thought above is only a qualitative analysis, and a more precise quantitative analysis should be explored further.

Nevertheless, the corona parameters (τ , kT_e and f_{sc}) change little during the soft-to-hard transition, although the inner part of the corona (from the NS surface to the corotation radius) has been expelled out the system. This finding implies that the structure and property of the corona have little dependence on the radial distance, and the whole distributing of the corona is stable in this region. Since the disk viscous power is a strong function of the radial distance and decays rapidly outwards, this stable corona is against the origin that the corona’s power comes from the thermal electrons from the disk’s viscous power. Thus, another origin of the corona—the magnetic field is favored, and it could be the reservoir depositing much more energy than the thermal energy content (Merloni & Fabian 2001).

In theory, the NS surface temperature is expected to increase as the accretion rate increases. However, the above results are obtained by the assumption that the NS surface emission has a mild change during the whole outburst. The small counts of the spectrum prevent us unfixing the NS surface parameters, due to the effective area is not big enough to distinguish the accretion disk and the NS surface emission. A larger detection area and broadband energy coverage may be satisfied by the next generation of Chinese mission of so-called eXTP (enhanced X-ray Timing and Polarimetry mission) (Zhang et al. 2019).

This work made use of the data and software from the Insight-HXMT mission, a project funded by China National Space Administration (CNSA) and the Chinese Academy of Sciences (CAS). This research has made use of data and software provided by of data obtained from the High Energy Astrophysics Science Archive Research Center (HEASARC), provided by NASA’s Goddard Space Flight Center. This work is supported by the National Key R&D Program of China (2021YFA0718500) and the National Natural Science Foundation of China under grants 11733009, U1838201, U1838202, U1938101, U2038101, 12130342, U1938107, 12173103. This work was partially supported by International

Partnership Program of Chinese Academy of Sciences (Grant No.113111KYSB20190020).

REFERENCES

- Arons, J. & Lea, S. M. 1976, *ApJ*, 207, 914
- Arnaud K. A., 1996, in Jacoby G. H., Barnes J., eds, *Astronomical Society of the Pacific Conference Series Vol. 101, Astronomical Data Analysis Software and Systems V.* p. 17
- Bozzo, E., Stella, L., Vietri, M., et al. 2009, *A&A*, 493, 809. doi:10.1051/0004-6361:200810658
- Bozzo, E., Ascenzi, S., Ducci, L., et al. 2018, *A&A*, 617, A126. doi:10.1051/0004-6361/201732004
- Campana, S., Stella, L., Mereghetti, S., et al. 2018, *A&A*, 610, A46. doi:10.1051/0004-6361/201730769
- Campana, S., & Stella, L. 2000, *ApJ*, 541, 849
- Chen, X., Zhang, S.-N., Ding, G.-Q. 2006, *ApJ*, 650, 299
- Chen, Y. P., Zhang, S., Ji, L., Zhang, S. N., et al. 2022a, *ApJ*, 936, 46
- Chen, Y. P., Zhang, S., Ji, L., Zhang, S. N., et al. 2022b, arXiv:2209.10721
- Cominsky, L., Jones, C., Forman, W., & Tananbaum, H. 1978, *ApJ*, 224, 46
- Corbet, R. H. D. 1996, *ApJL*, 457, L31
- Done, C., Gierliński, M., Kubota, A. 2007, , *A&ARv*, 15, 1
- Forman, W., Jones, C., Cominsky, L. et al. 1978, *ApJS*, 38, 357
- Cui, W. 1997, *ApJL*, 482, L163

- D’Angelo, C. R. & Spruit, H. C. 2012, MNRAS, 420, 416. doi:10.1111/j.1365-2966.2011.20046.x
- Fender R., & Belloni T., 2004, ARA&A, 42, 317
- Elsner, R. F. & Lamb, F. K. 1977, ApJ 215, 897
- Illarionov, A. F., Sunyaev, R. A., 1975. A&A 39, 185
- Kaastra, J. S.; Bleeker, J. A. M. 2016, A&A, 587, A151
- Lii, P. S., Romanova, M. M., Ustyugova, G. V., et al. 2014, MNRAS, 441, 86. doi:10.1093/mnras/stu495
- López-Navas, E., Degenaar, N., Parikh, A. S. et al., 2020, MNRAS, 493, 940
- Lamb, F. K., Pethick, C. J., & Pines, D. 1973, ApJ, 184, 271
- Li, Z. S., Yu, W. H., Lu, Y. Q., et al. 2022, ApJ, 935, 123
- Li, X. B., Li, X. F., Tan, Y. et al. 2020, JHEA, 27, 64
- Maccarone, T. J. & Coppi, P. S. 2003, A&A, 399, 1151
- Merloni, A., & Fabian, A. C. 2001, MNRAS, 321, 549
- Powell, C. R., Haswell, C. A., & Falanga, M. 2007, MNRAS, 374, 466
- Remillard, R. A., Loewenstein, M., Steiner, J. F. et al. 2022, AJ, 163, 130
- Romanova, M. M. & Owocki, S. P. 2015, SSRv, 191, 339. doi:10.1007/s11214-015-0200-9
- Stella, L., White, N. E., & Rosner, R. 1986, ApJ, 308, 669
- Thompson, T. W. J., Rothschild, R. E., Tomsick, J. A., & Marshall, H. L. 2005, ApJ, 42, 1261

- Tomsick, J. A., Gelino, D. M., & Kaaret, P. 2007, *ApJ*, 663, 461
- Ustyugova, G. V., Koldoba, A. V., Romanova, M. M., et al. 2006, *ApJ*, 646, 304.
doi:10.1086/503379
- Wilms, J., Allen, A., & McCray, R. 2000, *ApJ*, 542, 914
- Zand, J. J. M., Keek, L., Cumming, A., et al. 2009, *A&A*, 497, 469
- Zdziarski, A. A., Szanecki, M., Poutanen, J., Gierlinski, M., & Biernacki, P. 2020, *MNRAS*, 492, 5234
- Zhang, S. N., Yu, W., Zhang, W, 1998, *ApJL*, 494, L71
- Zhang, S. N., Santangelo, A., Feroci, M., et al. 2019, *Science China Physics, Mechanics & Astronomy*, Volume 62, Issue 2, article id. 29502, 25
- Zhang, S.-N., Li, T.-P., Lu, F.-J., et al. 2020, *SCPMA*, 63, 249502

Table 1: The results of the spectral fit of the NICER spectra in the 0.4–7 keV range with `cons*tbabs*thcomp*bb` at the onset of the outburst in 2021 and the extinction time of the outburst in 2022

No	Time	N_{H}	τ	kT_{e}	f_{sc}	kT_{bb}	R_{bb}	F_{bb}	F_{corona}	F_{total}	χ^2_{ν} (d.o.f.)
	MJD	10^{22} cm^{-2}		keV		keV	km	10^{-9}	10^{-9}	10^{-9}	
1	59376.74	0.39 ± 0.009	$1.5^{+8.2}_{-0.2}$	$64.01^{+27.39}_{-43.19}$	$0.97_{-0.2}$	$0.43^{+0.01}_{-0.01}$	$12.0^{+0.4}_{-0.4}$	$0.094^{+0.001}_{-0.001}$	$0.195^{+0.008}_{-0.011}$	$0.290^{+0.008}_{-0.011}$	0.65(136)
2	59801.32	0.39 ± 0.005	$2.3^{+6.7}_{-1.6}$	$45.82^{+179.90}_{-41.86}$	$0.77_{-0.2}$	$0.47^{+0.01}_{-0.01}$	$10.4^{+0.2}_{-0.2}$	$0.095^{+0.001}_{-0.001}$	$0.240^{+0.001}_{-0.001}$	$0.335^{+0.001}_{-0.001}$	0.74(109)

The onset of the outburst 2011 includes the NICER obsids 4202200101–42002200106, the extinction time of the outburst in 2022 includes the NICER obsids 4639010197–4639010210, as shown in the green boxes in Figure 1 and Figure 2. The model parameters: the optical depth τ , the electron temperature kT_{e} , the cover factor f_{sc} , the blackbody temperature kT_{bb} and the blackbody radius R_{bb} at a distance of 7.56 kpc, the bolometric flux of the blackbody F_{bb} , the bolometric flux of the corona F_{corona} , and the total bolometric flux F_{total} are in units of $10^{-9} \text{ erg/cm}^2/\text{s}$, reduced χ^2_{ν} and the degree of freedom (d.o.f.). Please note the energy range of the two stacked spectra—the onset of the outburst in 2011 and the extinction time of the outburst in 2022 (right) are truncated to 0.4–7 keV because of the high background level at $> 7 \text{ keV}$.

Table 2: The results of the spectral fit of the jointed observations of NICER, Insight-HXMT/LE, and Insight-HXMT/ME in the 0.4–20 keV range with `cons*tbabs*thcomp*(bb+diskbb)` during the outbursts in 2021 and 2022

No	HXMT obsid	Time MJD	NICER obsid	N_{H} 10^{22} cm^{-2}	τ	kT_{e} keV	f_{sc}	kT_{disk} keV	R_{disk} km	F_{disk} 10^{-9}	F_{corona} 10^{-9}	F_{total} 10^{-9}	χ^2_{ν} (d.o.f.)
1	P041401100101-20210707-01-01	59402.25	4202200123	0.52 ± 0.006	$13.1^{+0.3}_{-0.2}$	$2.47^{+0.05}_{-0.06}$	$1.00_{-0.02}$	$0.59^{+0.02}_{-0.02}$	$17.9^{+1.1}_{-0.9}$	$1.435^{+0.009}_{-0.007}$	$2.298^{+0.020}_{-0.021}$	$3.823^{+0.018}_{-0.020}$	1.05(181)
2	P041401101101-20210723-01-01	59418.48	4202200131	0.52 ± 0.008	$13.5^{+1.3}_{-1.1}$	$2.45^{+0.19}_{-0.16}$	$0.49^{+0.05}_{-0.05}$	$0.57^{+0.02}_{-0.02}$	$11.6^{+0.9}_{-0.8}$	$0.528^{+0.005}_{-0.005}$	$0.477^{+0.011}_{-0.011}$	$1.095^{+0.010}_{-0.010}$	0.90(170)
3	P051400200103-20220430-01-01	59699.41	4639010134	0.53 ± 0.009	$8.4^{+1.0}_{-1.0}$	$3.31^{+0.49}_{-0.36}$	$0.91_{-0.12}$	$0.67^{+0.04}_{-0.05}$	$14.5^{+1.7}_{-1.4}$	$1.591^{+0.014}_{-0.014}$	$1.433^{+0.041}_{-0.036}$	$3.114^{+0.035}_{-0.035}$	0.80(161)
4	P051400200401-20220503-01-01	59702.08	4639010135	0.52 ± 0.004	$12.2^{+0.4}_{-0.2}$	$2.55^{+0.07}_{-0.07}$	$1.00_{-0.02}$	$0.66^{+0.02}_{-0.02}$	$15.2^{+0.8}_{-0.7}$	$1.684^{+0.009}_{-0.008}$	$2.306^{+0.028}_{-0.019}$	$4.080^{+0.026}_{-0.017}$	1.02(188)
5	P051400200501-20220504-01-01	59703.07	4639010136	0.52 ± 0.005	$12.0^{+0.5}_{-0.5}$	$2.49^{+0.10}_{-0.09}$	$1.00_{-0.05}$	$0.66^{+0.03}_{-0.02}$	$14.8^{+0.8}_{-1.0}$	$1.538^{+0.009}_{-0.008}$	$1.944^{+0.019}_{-0.022}$	$3.572^{+0.017}_{-0.023}$	1.27(184)
6	P051400200602-20220505-01-01	59704.44	4639010137	0.51 ± 0.004	$11.3^{+0.3}_{-0.3}$	$2.80^{+0.07}_{-0.07}$	$1.00_{-0.01}$	$0.71^{+0.02}_{-0.02}$	$13.5^{+0.5}_{-0.5}$	$1.751^{+0.007}_{-0.007}$	$2.299^{+0.024}_{-0.020}$	$4.140^{+0.023}_{-0.019}$	1.14(188)
7	P051400200702-20220506-01-01	59705.20	4639010138	0.52 ± 0.004	$9.6^{+0.3}_{-0.4}$	$2.93^{+0.13}_{-0.09}$	$1.00_{-0.01}$	$0.65^{+0.01}_{-0.01}$	$15.2^{+0.5}_{-0.5}$	$1.579^{+0.007}_{-0.007}$	$1.679^{+0.017}_{-0.017}$	$3.348^{+0.016}_{-0.015}$	1.11(192)
8	P051400200802-20220507-01-01	59706.29	4639010139	0.53 ± 0.004	$10.6^{+0.4}_{-0.3}$	$2.81^{+0.10}_{-0.10}$	$1.00_{-0.04}$	$0.63^{+0.02}_{-0.01}$	$16.0^{+0.7}_{-0.9}$	$1.526^{+0.009}_{-0.008}$	$1.872^{+0.019}_{-0.024}$	$3.488^{+0.017}_{-0.022}$	1.18(187)

a : The model parameters: the optical depth τ , the electron temperature kT_{e} , the cover factor f_{sc} , the accretion disk temperature kT_{disk} and the inner disk radius R_{disk} at a distance of 7.56 kpc and in the face-on scenario (inclination angel $\theta=0$), the bolometric flux of the diskbb F_{diskbb} , the bolometric flux of the corona F_{diskbb} , and the total bolometric flux F_{total} are in units of $10^{-9} \text{ erg/cm}^2/\text{s}$, reduced χ^2_{ν} and the degree of freedom (d.o.f.).

Table 3:: The results of the spectral fit of the NICER spectra in the 0.4–10 keV range with
tbabs*thcomp*(bb+diskbb)

No	obsid	Time MJD	Exposure s	Rate cts/s	N_{H} 10^{22} cm^{-2}	τ	kT_{e} keV	f_{sc}	kT_{disk} keV	R_{disk} km	F_{disk} 10^{-9}	F_{corona} 10^{-9}	F_{total} 10^{-9}	χ^2_{ν} (d.o.f.)
1	4202200109	59382.45	2700	43.5	0.46 ± 0.021	$11.7^{+2.6}_{-4.6}$	$3.18^{+3.32}_{-0.64}$	$0.77^{+0.07}_{-0.06}$	$0.18^{+0.07}_{-0.06}$	$21.0^{+41.1}_{-5.6}$	$0.015^{+0.001}_{-0.001}$	$0.144^{+0.001}_{-0.001}$	$0.249^{+0.001}_{-0.001}$	0.64(121)
2	4202200110	59383.23	2430	46.8	0.43 ± 0.005	$18.5^{+1.3}_{-1.1}$	$2.02^{+0.08}_{-0.08}$	$0.67^{+0.04}_{-0.04}$	$0.06^{+0.01}_{-0.01}$	$223.1^{+2.3}_{-2.3}$	$0.012^{+0.001}_{-0.001}$	$0.140^{+0.001}_{-0.001}$	$0.243^{+0.001}_{-0.001}$	0.84(123)
3	4202200111	59384.00	2062	48.9	0.50 ± 0.020	$12.9^{+2.7}_{-3.3}$	$2.72^{+1.19}_{-0.44}$	$0.81^{+0.09}_{-0.08}$	$0.17^{+0.06}_{-0.12}$	$29.7^{+43.2}_{-10.9}$	$0.027^{+0.001}_{-0.001}$	$0.169^{+0.001}_{-0.001}$	$0.285^{+0.001}_{-0.001}$	1.18(118)
4	4202200112	59385.16	5585	58.1	0.54 ± 0.035	$7.9^{+2.1}_{-2.6}$	$5.06^{+2.04}_{-1.38}$	$1.00^{+0.06}_{-0.06}$	$0.16^{+0.08}_{-0.12}$	$47.3^{+49.2}_{-20.4}$	$0.047^{+0.001}_{-0.001}$	$0.267^{+0.001}_{-0.001}$	$0.404^{+0.001}_{-0.001}$	0.83(133)
5	4202200113	59386.33	2544	67.4	0.54 ± 0.020	$12.1^{+1.8}_{-2.0}$	$2.86^{+0.67}_{-0.38}$	$0.91^{+0.04}_{-0.09}$	$0.06^{+0.13}_{-0.05}$	$457.3^{+225.2}_{-225.2}$	$0.057^{+0.001}_{-0.001}$	$0.291^{+0.001}_{-0.001}$	$0.438^{+0.001}_{-0.001}$	1.07(125)
6	4202200114	59387.11	5027	76.7	0.57 ± 0.009	$11.9^{+1.0}_{-1.0}$	$3.05^{+0.36}_{-0.26}$	$0.95^{+0.06}_{-0.06}$	$0.09^{+0.01}_{-0.01}$	$206.2^{+0.5}_{-0.5}$	$0.073^{+0.001}_{-0.001}$	$0.364^{+0.001}_{-0.001}$	$0.528^{+0.001}_{-0.001}$	0.94(134)
7	4202200115	59390.26	1118	96.3	0.56 ± 0.010	$13.9^{+1.4}_{-0.4}$	$2.65^{+0.13}_{-0.25}$	$1.00^{+0.12}_{-0.12}$	$0.10^{+0.01}_{-0.01}$	$180.5^{+0.5}_{-0.5}$	$0.090^{+0.001}_{-0.001}$	$0.478^{+0.003}_{-0.003}$	$0.658^{+0.002}_{-0.002}$	1.02(120)
8	4202200116	59392.08	986	103.7	0.55 ± 0.020	$14.6^{+0.8}_{-0.8}$	$2.63^{+0.18}_{-0.14}$	$1.00^{+0.05}_{-0.05}$	$0.18^{+0.07}_{-0.07}$	$55.0^{+70.5}_{-20.2}$	$0.107^{+0.001}_{-0.001}$	$0.512^{+0.003}_{-0.003}$	$0.709^{+0.003}_{-0.003}$	0.86(114)
9	4202200119	59396.59	860	150.4	0.50 ± 0.048	$17.4^{+1.5}_{-1.7}$	$2.41^{+0.25}_{-0.16}$	$0.69^{+0.18}_{-0.20}$	$0.21^{+0.05}_{-0.02}$	$55.7^{+30.5}_{-17.8}$	$0.218^{+0.001}_{-0.001}$	$0.719^{+0.004}_{-0.004}$	$1.027^{+0.004}_{-0.004}$	0.81(121)
10	4202200120	59397.94	165	194.2	0.55 ± 0.071	$15.9^{+1.7}_{-1.9}$	$2.57^{+0.51}_{-0.30}$	$0.52^{+0.20}_{-0.21}$	$0.19^{+0.03}_{-0.03}$	$92.5^{+100.9}_{-27.8}$	$0.402^{+0.003}_{-0.004}$	$0.882^{+0.010}_{-0.010}$	$1.375^{+0.010}_{-0.010}$	0.98(96)
11	4202200121	59398.20	2146	233.5	0.52 ± 0.025	$14.3^{+0.7}_{-0.6}$	$2.95^{+0.18}_{-0.17}$	$0.57^{+0.04}_{-0.04}$	$0.27^{+0.02}_{-0.02}$	$52.9^{+13.8}_{-11.1}$	$0.480^{+0.001}_{-0.001}$	$1.029^{+0.004}_{-0.004}$	$1.599^{+0.004}_{-0.004}$	0.85(135)
12	4202200122	59401.69	1555	666.3	0.51 ± 0.007	$14.4^{+1.9}_{-1.0}$	$2.16^{+0.13}_{-0.14}$	$0.91^{+0.16}_{-0.16}$	$0.61^{+0.07}_{-0.06}$	$17.4^{+3.8}_{-2.6}$	$1.527^{+0.003}_{-0.003}$	$1.979^{+0.008}_{-0.008}$	$3.597^{+0.007}_{-0.007}$	0.60(140)
13	4202200123	59402.29	1745	654.2	0.51 ± 0.007	$16.3^{+2.2}_{-1.3}$	$2.05^{+0.12}_{-0.12}$	$0.81^{+0.14}_{-0.15}$	$0.62^{+0.07}_{-0.07}$	$16.9^{+4.4}_{-2.4}$	$1.518^{+0.003}_{-0.003}$	$2.004^{+0.007}_{-0.007}$	$3.612^{+0.007}_{-0.007}$	0.64(142)
14	4202200124	59403.06	2152	566.2	0.51 ± 0.007	$17.1^{+7.0}_{-2.2}$	$1.92^{+0.07}_{-0.19}$	$0.59^{+0.13}_{-0.24}$	$0.70^{+0.08}_{-0.05}$	$13.1^{+1.7}_{-1.9}$	$1.499^{+0.127}_{-0.094}$	$1.275^{+0.127}_{-0.095}$	$2.864^{+0.006}_{-0.011}$	0.56(141)
15	4202200126	59405.06	3526	556.9	0.51 ± 0.006	$17.7^{+5.4}_{-2.0}$	$1.97^{+0.12}_{-0.16}$	$0.58^{+0.12}_{-0.19}$	$0.71^{+0.07}_{-0.04}$	$12.6^{+1.5}_{-1.7}$	$1.472^{+0.003}_{-0.003}$	$1.373^{+0.006}_{-0.006}$	$2.936^{+0.005}_{-0.005}$	0.64(147)
16	4202200127	59406.47	3064	524.0	0.51 ± 0.006	$16.4^{+3.2}_{-1.6}$	$2.07^{+0.13}_{-0.15}$	$0.67^{+0.11}_{-0.16}$	$0.68^{+0.06}_{-0.05}$	$12.9^{+1.6}_{-1.6}$	$1.332^{+0.003}_{-0.003}$	$1.406^{+0.006}_{-0.006}$	$2.829^{+0.005}_{-0.005}$	0.82(146)
17	4202200128	59407.50	2389	491.3	0.51 ± 0.007	$14.3^{+2.7}_{-1.4}$	$2.30^{+0.18}_{-0.21}$	$0.73^{+0.11}_{-0.16}$	$0.67^{+0.06}_{-0.04}$	$13.0^{+1.7}_{-1.6}$	$1.226^{+0.003}_{-0.003}$	$1.347^{+0.006}_{-0.006}$	$2.663^{+0.005}_{-0.005}$	0.77(142)
18	4202200129	59408.47	3469	458.6	0.51 ± 0.006	$23.6^{+5.1}_{-5.1}$	$1.76^{+0.13}_{-0.19}$	$0.34^{+0.14}_{-0.22}$	$0.75^{+0.11}_{-0.05}$	$10.5^{+1.3}_{-1.9}$	$1.308^{+0.003}_{-0.003}$	$0.885^{+0.005}_{-0.005}$	$2.283^{+0.004}_{-0.004}$	0.56(144)
19	4202200130	59417.93	790	218.6	0.50 ± 0.009	$22.3^{+13.2}_{-5.6}$	$1.83^{+0.29}_{-0.20}$	$0.26^{+0.10}_{-0.10}$	$0.60^{+0.04}_{-0.04}$	$10.8^{+1.3}_{-1.1}$	$0.555^{+0.002}_{-0.002}$	$0.362^{+0.004}_{-0.004}$	$1.007^{+0.004}_{-0.004}$	0.82(118)
20	4202200131	59418.05	1927	220.5	0.51 ± 0.009	$15.8^{+3.0}_{-2.4}$	$2.16^{+0.29}_{-0.21}$	$0.43^{+0.08}_{-0.08}$	$0.57^{+0.03}_{-0.03}$	$11.9^{+1.2}_{-1.0}$	$0.527^{+0.002}_{-0.002}$	$0.441^{+0.003}_{-0.003}$	$1.057^{+0.003}_{-0.003}$	0.74(130)
21	4202200132	59450.90	1003	57.9	0.59 ± 0.009	$12.5^{+1.5}_{-1.2}$	$2.67^{+0.31}_{-0.27}$	$0.93^{+0.09}_{-0.09}$	$0.11^{+0.01}_{-0.01}$	$101.2^{+0.6}_{-0.6}$	$0.045^{+0.001}_{-0.001}$	$0.232^{+0.002}_{-0.002}$	$0.367^{+0.002}_{-0.002}$	1.01(111)
22	4202200133	59451.48	2517	58.9	0.58 ± 0.008	$12.9^{+1.6}_{-1.3}$	$2.80^{+0.35}_{-0.29}$	$0.82^{+0.06}_{-0.07}$	$0.11^{+0.01}_{-0.01}$	$103.7^{+0.4}_{-0.4}$	$0.046^{+0.001}_{-0.001}$	$0.242^{+0.001}_{-0.001}$	$0.378^{+0.001}_{-0.001}$	0.88(121)
23	4202200134	59455.23	1153	53.4	0.58 ± 0.056	$10.7^{+3.1}_{-1.3}$	$2.96^{+0.31}_{-0.62}$	$1.00^{+0.12}_{-0.12}$	$0.16^{+0.07}_{-0.15}$	$44.0^{+103.2}_{-20.7}$	$0.038^{+0.001}_{-0.001}$	$0.181^{+0.002}_{-0.002}$	$0.308^{+0.002}_{-0.002}$	0.92(112)
24	4202200135	59624.52	6923	602.4	0.51 ± 0.006	$18.5^{+13.8}_{-2.5}$	$1.85^{+0.11}_{-0.12}$	$0.50^{+0.13}_{-0.27}$	$0.75^{+0.09}_{-0.04}$	$12.0^{+1.3}_{-1.3}$	$1.667^{+0.003}_{-0.003}$	$1.240^{+0.005}_{-0.005}$	$2.998^{+0.005}_{-0.005}$	0.58(154)
25	4202200136	59625.11	3908	645.6	0.51 ± 0.006	$16.6^{+3.5}_{-1.3}$	$1.98^{+0.09}_{-0.13}$	$0.74^{+0.06}_{-0.20}$	$0.68^{+0.08}_{-0.05}$	$14.2^{+1.9}_{-2.1}$	$1.605^{+0.003}_{-0.003}$	$1.776^{+0.006}_{-0.006}$	$3.470^{+0.006}_{-0.006}$	0.55(150)
26	4202200137	59626.01	1842	645.5	0.51 ± 0.006	$24.0^{+0.17}_{-6.5}$	$1.74^{+0.17}_{-0.16}$	$0.37^{+0.24}_{-0.21}$	$0.79^{+0.13}_{-0.08}$	$11.4^{+2.4}_{-2.2}$	$1.880^{+0.004}_{-0.004}$	$1.339^{+0.007}_{-0.007}$	$3.309^{+0.006}_{-0.006}$	0.66(141)
27	4202200138	59627.05	4099	652.3	0.51 ± 0.006	$16.5^{+8.9}_{-2.0}$	$1.98^{+0.13}_{-0.21}$	$0.61^{+0.14}_{-0.30}$	$0.75^{+0.10}_{-0.05}$	$12.5^{+1.6}_{-3.1}$	$1.762^{+0.003}_{-0.003}$	$1.516^{+0.006}_{-0.006}$	$3.368^{+0.005}_{-0.005}$	0.62(150)
28	4202200139	59628.01	1110	661.9	0.52 ± 0.008	$14.3^{+2.0}_{-1.2}$	$2.06^{+0.15}_{-0.15}$	$0.89^{+0.07}_{-0.18}$	$0.59^{+0.07}_{-0.07}$	$18.7^{+4.9}_{-2.8}$	$1.508^{+0.141}_{-0.109}$	$1.817^{+0.146}_{-0.116}$	$3.415^{+0.036}_{-0.038}$	0.66(137)
29	4202200140	59629.05	2372	627.8	0.51 ± 0.007	$13.0^{+1.6}_{-1.2}$	$2.19^{+0.18}_{-0.15}$	$0.88^{+0.05}_{-0.15}$	$0.63^{+0.05}_{-0.06}$	$16.4^{+3.6}_{-1.9}$	$1.496^{+0.104}_{-0.096}$	$1.586^{+0.106}_{-0.100}$	$3.172^{+0.023}_{-0.029}$	0.73(144)
30	5202200102	59640.10	7562	589.2	0.50 ± 0.004	$20.4^{+0.12}_{-3.6}$	$1.79^{+0.12}_{-0.19}$	$0.43^{+0.15}_{-0.30}$	$0.75^{+0.14}_{-0.05}$	$11.8^{+1.6}_{-2.3}$	$1.643^{+0.269}_{-0.113}$	$1.127^{+0.269}_{-0.113}$	$2.859^{+0.009}_{-0.009}$	0.52(147)
31	5202200103	59641.33	1982	584.4	0.50 ± 0.009	$13.4^{+3.5}_{-1.8}$	$2.17^{+0.23}_{-0.24}$	$0.71^{+0.15}_{-0.21}$	$0.68^{+0.06}_{-0.05}$	$13.9^{+1.9}_{-1.7}$	$1.507^{+0.090}_{-0.089}$	$1.246^{+0.095}_{-0.093}$	$2.842^{+0.031}_{-0.028}$	0.66(136)
32	5202200104	59642.04	12902	679.9	0.50 ± 0.005	$20.4^{+43.5}_{-3.1}$	$1.86^{+0.10}_{-0.27}$	$0.50^{+0.15}_{-0.37}$	$0.78^{+0.15}_{-0.06}$	$11.7^{+1.7}_{-2.5}$	$1.917^{+0.334}_{-0.150}$	$1.567^{+0.334}_{-0.150}$	$3.574^{+0.013}_{-0.011}$	0.48(152)
33	5202200105	59643.01	5594	698.2	0.50 ± 0.005	$24.2^{+0.14}_{-6.1}$	$1.76^{+0.14}_{-0.14}$	$0.35^{+0.20}_{-0.20}$	$0.82^{+0.07}_{-0.07}$	$11.2^{+1.8}_{-1.7}$	$2.080^{+0.296}_{-0.170}$	$1.381^{+0.296}_{-0.170}$	$3.550^{+0.011}_{-0.011}$	0.51(148)
34	5202200106	59647.09	1082	785.3	0.50 ± 0.007	$16.1^{+0.25}_{-2.7}$	$2.13^{+0.25}_{-0.37}$	$0.72^{+0.26}_{-0.57}$	$0.77^{+0.29}_{-0.11}$	$12.7^{+4.0}_{-3.8}$	$2.128^{+0.772}_{-0.272}$	$2.176^{+0.777}_{-0.276}$	$4.395^{+0.089}_{-0.044}$	0.92(135)
35	5202200107	59648.23	2813	731.0	0.50 ± 0.006	$20.1^{+0.14}_{-3.9}$	$1.80^{+0.14}_{-0.21}$	$0.47^{+0.20}_{-0.24}$	$0.78^{+0.20}_{-0.07}$	$12.3^{+2.0}_{-2.9}$	$2.087^{+0.620}_{-0.166}$	$1.531^{+0.621}_{-0.167}$	$3.708^{+0.020}_{-0.014}$	0.53(145)

Table 3:: The results of the spectral fit of the NICER spectra in the 0.4–10 keV range with
tbabs*thcomp*(bb+diskbb)

No	obsid	Time MJD	Exposure s	Rate cts/s	N_{H} 10^{22} cm^{-2}	τ	kT_{e} keV	f_{sc}	kT_{disk} keV	R_{disk} km	F_{disk} 10^{-9}	F_{corona} 10^{-9}	F_{total} 10^{-9}	χ^2_{ν} (d.o.f.)
36	5202200108	59649.07	2867	720.3	0.51 ± 0.006	$15.5^{+3.4}_{-1.4}$	$1.98^{+0.11}_{-0.15}$	$0.76^{+0.14}_{-0.22}$	$0.67^{+0.08}_{-0.05}$	$15.6^{+2.5}_{-2.3}$	$1.819^{+0.141}_{-0.133}$	$1.792^{+0.144}_{-0.135}$	$3.701^{+0.029}_{-0.024}$	0.51(145)
37	5202200110	59653.77	793	754.4	0.52 ± 0.008	$12.1^{+3.1}_{-1.7}$	$2.35^{+0.36}_{-0.30}$	$0.88^{+0.25}_{-0.25}$	$0.70^{+0.08}_{-0.07}$	$14.9^{+3.0}_{-2.1}$	$1.938^{+0.184}_{-0.124}$	$1.895^{+0.192}_{-0.136}$	$3.924^{+0.057}_{-0.058}$	0.86(135)
38	5202200111	59656.69	1597	743.5	0.51 ± 0.007	$17.6^{+2.8}_{-2.8}$	$1.90^{+0.16}_{-0.28}$	$0.63^{+0.21}_{-0.46}$	$0.74^{+0.23}_{-0.08}$	$13.3^{+2.7}_{-3.3}$	$2.001^{+0.646}_{-0.178}$	$1.803^{+0.647}_{-0.180}$	$3.894^{+0.033}_{-0.024}$	0.59(141)
39	5202200114	59659.02	6348	751.7	0.51 ± 0.006	$17.8^{+4.4}_{-1.4}$	$1.93^{+0.08}_{-0.12}$	$0.69^{+0.11}_{-0.21}$	$0.72^{+0.09}_{-0.05}$	$14.0^{+1.8}_{-2.1}$	$1.959^{+0.168}_{-0.136}$	$2.039^{+0.170}_{-0.137}$	$4.088^{+0.023}_{-0.018}$	0.47(153)
40	5202200116	59661.01	4471	742.4	0.51 ± 0.006	$15.6^{+3.3}_{-1.2}$	$2.03^{+0.10}_{-0.15}$	$0.79^{+0.13}_{-0.22}$	$0.69^{+0.08}_{-0.06}$	$14.8^{+2.3}_{-2.3}$	$1.880^{+0.150}_{-0.143}$	$1.948^{+0.153}_{-0.145}$	$3.918^{+0.028}_{-0.023}$	0.68(150)
41	4639010101	59663.59	7446	704.0	0.51 ± 0.006	$17.3^{+6.5}_{-1.7}$	$1.94^{+0.09}_{-0.16}$	$0.62^{+0.12}_{-0.25}$	$0.75^{+0.09}_{-0.04}$	$12.9^{+1.4}_{-1.9}$	$1.936^{+0.161}_{-0.131}$	$1.650^{+0.163}_{-0.132}$	$3.675^{+0.020}_{-0.015}$	0.54(153)
42	4639010103	59665.01	5134	638.6	0.51 ± 0.006	$12.4^{+2.9}_{-1.7}$	$2.42^{+0.28}_{-0.28}$	$0.68^{+0.12}_{-0.17}$	$0.73^{+0.05}_{-0.04}$	$13.0^{+1.3}_{-1.3}$	$1.735^{+0.082}_{-0.073}$	$1.372^{+0.091}_{-0.081}$	$3.197^{+0.039}_{-0.037}$	0.54(149)
43	4639010105	59667.21	1529	719.9	0.51 ± 0.008	$17.6^{+3.7}_{-1.7}$	$1.85^{+0.10}_{-0.12}$	$0.76^{+0.16}_{-0.21}$	$0.66^{+0.08}_{-0.08}$	$15.9^{+3.9}_{-2.4}$	$1.745^{+0.174}_{-0.166}$	$1.965^{+0.177}_{-0.167}$	$3.800^{+0.030}_{-0.024}$	0.76(139)
44	4639010106	59668.16	3078	746.1	0.51 ± 0.006	$16.9^{+7.5}_{-1.7}$	$1.94^{+0.11}_{-0.18}$	$0.71^{+0.15}_{-0.06}$	$0.73^{+0.12}_{-0.06}$	$13.8^{+2.2}_{-2.6}$	$1.990^{+0.228}_{-0.185}$	$1.895^{+0.230}_{-0.186}$	$3.975^{+0.028}_{-0.020}$	0.66(149)
45	4639010107	59669.52	4371	757.2	0.51 ± 0.005	$17.2^{+2.2}_{-1.2}$	$1.88^{+0.07}_{-0.08}$	$0.79^{+0.13}_{-0.15}$	$0.64^{+0.06}_{-0.06}$	$17.3^{+3.7}_{-2.3}$	$1.792^{+0.141}_{-0.141}$	$2.138^{+0.143}_{-0.142}$	$4.020^{+0.026}_{-0.021}$	0.58(152)
46	4639010108	59670.63	4969	720.9	0.51 ± 0.006	$15.1^{+3.8}_{-1.5}$	$2.02^{+0.12}_{-0.17}$	$0.72^{+0.14}_{-0.22}$	$0.70^{+0.07}_{-0.05}$	$14.4^{+2.1}_{-2.0}$	$1.855^{+0.137}_{-0.125}$	$1.651^{+0.140}_{-0.127}$	$3.596^{+0.026}_{-0.022}$	0.67(151)
47	4639010109	59671.65	3391	718.2	0.51 ± 0.005	$20.6^{+3.5}_{-3.5}$	$1.79^{+0.12}_{-0.20}$	$0.52^{+0.19}_{-0.38}$	$0.77^{+0.16}_{-0.07}$	$12.5^{+2.1}_{-2.8}$	$1.996^{+0.379}_{-0.179}$	$1.643^{+0.380}_{-0.179}$	$3.729^{+0.020}_{-0.013}$	0.69(149)
48	4639010110	59672.70	2900	728.1	0.51 ± 0.006	$13.5^{+2.2}_{-1.0}$	$2.38^{+0.16}_{-0.21}$	$0.87^{+0.12}_{-0.19}$	$0.68^{+0.08}_{-0.06}$	$15.0^{+2.4}_{-2.2}$	$1.802^{+0.132}_{-0.131}$	$2.119^{+0.139}_{-0.137}$	$4.011^{+0.044}_{-0.043}$	0.57(147)
49	4639010111	59673.58	3561	660.2	0.51 ± 0.006	$16.3^{+4.5}_{-1.7}$	$1.94^{+0.11}_{-0.16}$	$0.64^{+0.13}_{-0.21}$	$0.69^{+0.07}_{-0.04}$	$14.4^{+1.8}_{-1.9}$	$1.734^{+0.124}_{-0.102}$	$1.497^{+0.126}_{-0.104}$	$3.321^{+0.024}_{-0.020}$	0.51(148)
50	5202200118	59676.11	583	705.7	0.51 ± 0.007	$15.7^{+6.2}_{-1.8}$	$1.96^{+0.17}_{-0.22}$	$0.84^{+0.35}_{-0.35}$	$0.66^{+0.13}_{-0.09}$	$15.8^{+4.0}_{-3.3}$	$1.707^{+0.263}_{-0.191}$	$1.923^{+0.267}_{-0.195}$	$3.721^{+0.047}_{-0.039}$	0.80(132)
51	4639010114	59676.55	4910	707.7	0.50 ± 0.006	$13.9^{+3.4}_{-1.3}$	$2.41^{+0.18}_{-0.24}$	$0.76^{+0.12}_{-0.21}$	$0.77^{+0.09}_{-0.05}$	$12.1^{+1.5}_{-1.7}$	$1.912^{+0.138}_{-0.122}$	$1.970^{+0.146}_{-0.128}$	$3.972^{+0.048}_{-0.040}$	0.58(153)
52	4639010117	59679.73	3162	680.7	0.51 ± 0.006	$16.4^{+4.5}_{-1.8}$	$2.00^{+0.13}_{-0.16}$	$0.65^{+0.13}_{-0.20}$	$0.71^{+0.07}_{-0.05}$	$13.2^{+1.7}_{-1.7}$	$1.619^{+0.117}_{-0.099}$	$1.489^{+0.120}_{-0.102}$	$3.199^{+0.027}_{-0.022}$	0.62(146)
53	4639010118	59680.56	4600	596.1	0.51 ± 0.006	$14.4^{+1.7}_{-1.2}$	$2.13^{+0.13}_{-0.13}$	$0.78^{+0.12}_{-0.13}$	$0.65^{+0.05}_{-0.05}$	$14.9^{+2.4}_{-1.6}$	$1.458^{+0.082}_{-0.085}$	$1.540^{+0.087}_{-0.088}$	$3.089^{+0.027}_{-0.024}$	0.46(150)
54	4639010120	59682.42	4339	641.5	0.51 ± 0.006	$19.3^{+11.6}_{-3.5}$	$1.95^{+0.16}_{-0.16}$	$0.50^{+0.19}_{-0.24}$	$0.80^{+0.07}_{-0.07}$	$11.1^{+1.9}_{-1.7}$	$1.807^{+0.227}_{-0.129}$	$1.551^{+0.229}_{-0.130}$	$3.448^{+0.028}_{-0.017}$	0.53(151)
55	4639010121	59683.28	4559	638.9	0.51 ± 0.006	$17.9^{+5.4}_{-1.8}$	$1.88^{+0.09}_{-0.13}$	$0.61^{+0.12}_{-0.21}$	$0.72^{+0.08}_{-0.04}$	$13.1^{+1.5}_{-1.8}$	$1.698^{+0.138}_{-0.100}$	$1.529^{+0.139}_{-0.101}$	$3.317^{+0.018}_{-0.015}$	0.61(151)
56	4639010122	59684.05	3881	595.5	0.51 ± 0.006	$13.6^{+3.2}_{-1.8}$	$2.22^{+0.23}_{-0.23}$	$0.64^{+0.12}_{-0.17}$	$0.71^{+0.05}_{-0.04}$	$13.1^{+1.4}_{-1.3}$	$1.601^{+0.081}_{-0.069}$	$1.258^{+0.086}_{-0.074}$	$2.949^{+0.029}_{-0.027}$	0.56(148)
57	4639010123	59685.01	1927	673.2	0.51 ± 0.007	$14.0^{+1.4}_{-1.1}$	$2.24^{+0.15}_{-0.20}$	$0.89^{+0.42}_{-0.17}$	$0.65^{+0.09}_{-0.06}$	$15.8^{+3.2}_{-2.7}$	$1.624^{+0.138}_{-0.139}$	$1.951^{+0.145}_{-0.144}$	$3.665^{+0.042}_{-0.038}$	0.58(143)
58	4639010124	59686.63	179	653.2	0.51 ± 0.009	$27.7^{+3.7}_{-13.5}$	$1.73^{+0.46}_{-0.16}$	$0.28^{+0.42}_{-0.17}$	$0.83^{+0.11}_{-0.13}$	$10.9^{+2.7}_{-1.8}$	$1.990^{+0.263}_{-0.273}$	$1.235^{+0.278}_{-0.276}$	$3.314^{+0.091}_{-0.040}$	0.83(114)
59	4639010125	59687.85	507	653.5	0.51 ± 0.008	$16.9^{+3.7}_{-2.0}$	$1.90^{+0.16}_{-0.16}$	$0.79^{+0.20}_{-0.22}$	$0.62^{+0.08}_{-0.09}$	$16.7^{+5.6}_{-2.7}$	$1.521^{+0.167}_{-0.170}$	$1.856^{+0.172}_{-0.174}$	$3.468^{+0.044}_{-0.039}$	0.83(131)
60	4639010128	59691.03	2047	625.7	0.51 ± 0.006	$20.1^{+4.1}_{-4.1}$	$1.87^{+0.17}_{-0.23}$	$0.48^{+0.20}_{-0.38}$	$0.79^{+0.18}_{-0.07}$	$11.3^{+2.0}_{-2.6}$	$1.787^{+0.348}_{-0.147}$	$1.415^{+0.349}_{-0.148}$	$3.292^{+0.028}_{-0.017}$	0.73(142)
61	4639010129	59692.05	1393	631.5	0.50 ± 0.007	$17.1^{+2.8}_{-2.8}$	$1.96^{+0.19}_{-0.30}$	$0.66^{+0.23}_{-0.53}$	$0.73^{+0.21}_{-0.09}$	$12.5^{+3.3}_{-3.3}$	$1.666^{+0.488}_{-0.179}$	$1.591^{+0.489}_{-0.180}$	$3.347^{+0.036}_{-0.025}$	0.69(138)
62	4639010130	59694.05	3235	542.8	0.51 ± 0.006	$13.8^{+3.5}_{-1.9}$	$2.18^{+0.24}_{-0.23}$	$0.59^{+0.13}_{-0.16}$	$0.70^{+0.05}_{-0.04}$	$12.9^{+1.3}_{-1.3}$	$1.475^{+0.069}_{-0.063}$	$1.086^{+0.075}_{-0.067}$	$2.651^{+0.030}_{-0.025}$	0.77(144)
63	4639010132	59696.05	1896	554.9	0.51 ± 0.007	$15.6^{+6.0}_{-2.4}$	$1.97^{+0.20}_{-0.21}$	$0.56^{+0.15}_{-0.21}$	$0.70^{+0.06}_{-0.04}$	$13.1^{+1.6}_{-1.6}$	$1.506^{+0.106}_{-0.076}$	$1.094^{+0.109}_{-0.079}$	$2.690^{+0.028}_{-0.020}$	0.74(140)
64	4639010133	59698.37	1799	635.5	0.51 ± 0.007	$15.7^{+4.0}_{-1.8}$	$1.98^{+0.15}_{-0.16}$	$0.70^{+0.15}_{-0.21}$	$0.67^{+0.07}_{-0.05}$	$14.7^{+2.3}_{-2.0}$	$1.621^{+0.126}_{-0.110}$	$1.534^{+0.130}_{-0.113}$	$3.244^{+0.032}_{-0.025}$	0.61(141)
65	4639010134	59700.05	450	598.4	0.52 ± 0.007	$24.3^{+3.1}_{-9.4}$	$1.68^{+0.31}_{-0.17}$	$0.30^{+0.30}_{-0.20}$	$0.77^{+0.11}_{-0.08}$	$11.6^{+2.5}_{-1.8}$	$1.778^{+0.230}_{-0.169}$	$1.001^{+0.233}_{-0.170}$	$2.869^{+0.042}_{-0.021}$	0.66(125)
66	4639010135	59702.11	2992	704.9	0.51 ± 0.006	$15.8^{+3.1}_{-1.3}$	$2.09^{+0.11}_{-0.15}$	$0.78^{+0.12}_{-0.20}$	$0.70^{+0.08}_{-0.06}$	$14.4^{+2.2}_{-2.1}$	$1.789^{+0.146}_{-0.129}$	$1.999^{+0.149}_{-0.132}$	$3.878^{+0.031}_{-0.028}$	0.56(144)
67	4639010136	59703.21	2215	628.6	0.51 ± 0.006	$17.4^{+8.6}_{-2.1}$	$1.94^{+0.13}_{-0.19}$	$0.65^{+0.15}_{-0.30}$	$0.73^{+0.11}_{-0.06}$	$12.8^{+2.0}_{-2.2}$	$1.716^{+0.200}_{-0.136}$	$1.586^{+0.202}_{-0.138}$	$3.393^{+0.027}_{-0.020}$	0.54(144)
68	4639010137	59704.05	2446	702.2	0.51 ± 0.006	$17.0^{+6.4}_{-1.6}$	$2.00^{+0.10}_{-0.18}$	$0.73^{+0.13}_{-0.29}$	$0.71^{+0.12}_{-0.06}$	$13.7^{+2.1}_{-2.2}$	$1.837^{+0.203}_{-0.161}$	$1.929^{+0.205}_{-0.163}$	$3.857^{+0.031}_{-0.026}$	0.66(147)
69	4639010138	59705.08	4848	630.9	0.51 ± 0.006	$15.6^{+4.3}_{-1.8}$	$1.99^{+0.13}_{-0.16}$	$0.62^{+0.13}_{-0.19}$	$0.72^{+0.06}_{-0.04}$	$13.2^{+1.5}_{-1.6}$	$1.704^{+0.109}_{-0.093}$	$1.347^{+0.110}_{-0.095}$	$3.141^{+0.019}_{-0.021}$	0.58(152)
70	4639010139	59706.04	2998	631.1	0.51 ± 0.006	$17.0^{+6.2}_{-2.1}$	$1.98^{+0.13}_{-0.18}$	$0.58^{+0.13}_{-0.22}$	$0.73^{+0.08}_{-0.04}$	$12.8^{+1.5}_{-1.7}$	$1.726^{+0.137}_{-0.100}$	$1.446^{+0.140}_{-0.102}$	$3.261^{+0.026}_{-0.020}$	0.65(147)

Table 3:: The results of the spectral fit of the NICER spectra in the 0.4–10 keV range with
tbabs*thcomp*(bb+diskbb)

No	obsid	Time MJD	Exposure s	Rate cts/s	N_{H} 10^{22} cm^{-2}	τ	kT_{e} keV	f_{sc}	kT_{disk} keV	R_{disk} km	F_{disk} 10^{-9}	F_{corona} 10^{-9}	F_{total} 10^{-9}	χ^2_{ν} (d.o.f.)
71	4639010140	59715.35	5811	477.8	0.51 ± 0.006	$13.8^{+2.2}_{-1.9}$	$2.37^{+0.27}_{-0.20}$	$0.50^{+0.09}_{-0.09}$	$0.69^{+0.03}_{-0.03}$	$12.6^{+1.0}_{-0.8}$	$1.301^{+0.039}_{-0.032}$	$0.963^{+0.049}_{-0.040}$	$2.353^{+0.030}_{-0.025}$	0.54(149)
72	4639010141	59718.12	4741	581.1	0.51 ± 0.006	$17.7^{+6.1}_{-2.0}$	$1.97^{+0.11}_{-0.16}$	$0.59^{+0.12}_{-0.21}$	$0.74^{+0.08}_{-0.05}$	$12.0^{+1.4}_{-1.7}$	$1.576^{+0.129}_{-0.093}$	$1.406^{+0.131}_{-0.095}$	$3.072^{+0.020}_{-0.018}$	0.53(151)
73	4639010143	59719.99	3886	583.8	0.51 ± 0.006	$18.7^{+10.1}_{-2.3}$	$1.89^{+0.11}_{-0.17}$	$0.53^{+0.12}_{-0.24}$	$0.73^{+0.09}_{-0.04}$	$12.2^{+1.3}_{-1.8}$	$1.604^{+0.154}_{-0.099}$	$1.325^{+0.154}_{-0.100}$	$3.019^{+0.014}_{-0.015}$	0.58(148)
74	4639010144	59721.05	5045	614.2	0.51 ± 0.007	$14.6^{+2.7}_{-1.3}$	$2.17^{+0.13}_{-0.17}$	$0.73^{+0.11}_{-0.17}$	$0.70^{+0.06}_{-0.04}$	$13.4^{+1.6}_{-1.6}$	$1.592^{+0.096}_{-0.089}$	$1.557^{+0.100}_{-0.092}$	$3.240^{+0.028}_{-0.025}$	0.58(152)
75	4639010145	59722.33	6456	523.8	0.50 ± 0.006	$15.5^{+4.0}_{-1.9}$	$2.04^{+0.15}_{-0.17}$	$0.52^{+0.11}_{-0.15}$	$0.72^{+0.05}_{-0.03}$	$12.2^{+1.0}_{-1.1}$	$1.441^{+0.067}_{-0.055}$	$1.014^{+0.070}_{-0.058}$	$2.545^{+0.019}_{-0.017}$	0.66(151)
76	4639010147	59724.01	7083	565.7	0.51 ± 0.006	$16.0^{+4.3}_{-2.2}$	$2.00^{+0.16}_{-0.16}$	$0.51^{+0.12}_{-0.16}$	$0.73^{+0.05}_{-0.04}$	$12.2^{+1.2}_{-1.1}$	$1.573^{+0.083}_{-0.064}$	$1.082^{+0.085}_{-0.066}$	$2.745^{+0.020}_{-0.015}$	0.67(153)
77	4639010148	59725.10	302	603.0	0.51 ± 0.008	$30.5^{+15.1}_{-1.1}$	$1.62^{+0.18}_{-0.14}$	$0.24^{+0.39}_{-0.13}$	$0.80^{+0.09}_{-0.12}$	$11.1^{+3.1}_{-3.0}$	$1.854^{+0.455}_{-0.271}$	$0.995^{+0.456}_{-0.272}$	$2.938^{+0.032}_{-0.026}$	0.82(119)
78	4639010149	59728.83	1705	652.6	0.51 ± 0.006	$13.9^{+3.6}_{-1.5}$	$2.32^{+0.22}_{-0.25}$	$0.78^{+0.14}_{-0.23}$	$0.72^{+0.08}_{-0.06}$	$13.2^{+2.0}_{-2.0}$	$1.708^{+0.142}_{-0.120}$	$1.799^{+0.151}_{-0.128}$	$3.597^{+0.049}_{-0.043}$	0.64(142)
79	4639010150	59729.09	4382	612.0	0.51 ± 0.004	$17.7^{+8.1}_{-2.0}$	$1.92^{+0.11}_{-0.18}$	$0.55^{+0.11}_{-0.23}$	$0.73^{+0.08}_{-0.04}$	$12.8^{+1.3}_{-1.9}$	$1.683^{+0.140}_{-0.094}$	$1.339^{+0.141}_{-0.096}$	$3.112^{+0.015}_{-0.019}$	0.59(150)
80	4639010151	59730.06	2401	578.5	0.51 ± 0.007	$12.6^{+1.9}_{-1.4}$	$2.32^{+0.24}_{-0.21}$	$0.81^{+0.14}_{-0.15}$	$0.65^{+0.05}_{-0.05}$	$14.8^{+2.3}_{-1.6}$	$1.437^{+0.077}_{-0.079}$	$1.418^{+0.085}_{-0.085}$	$2.945^{+0.035}_{-0.032}$	0.61(143)
81	4639010153	59732.96	1963	586.6	0.51 ± 0.007	$13.2^{+1.6}_{-1.3}$	$2.35^{+0.22}_{-0.18}$	$0.87^{+0.15}_{-0.15}$	$0.65^{+0.06}_{-0.07}$	$14.7^{+3.2}_{-1.8}$	$1.403^{+0.100}_{-0.098}$	$1.675^{+0.108}_{-0.104}$	$3.168^{+0.041}_{-0.035}$	0.63(142)
82	4639010154	59733.09	2840	584.9	0.51 ± 0.006	$18.4^{+5.9}_{-2.1}$	$1.90^{+0.11}_{-0.14}$	$0.59^{+0.12}_{-0.20}$	$0.71^{+0.08}_{-0.05}$	$12.9^{+1.7}_{-1.8}$	$1.543^{+0.129}_{-0.098}$	$1.453^{+0.131}_{-0.100}$	$3.085^{+0.022}_{-0.018}$	0.55(146)
83	4639010156	59735.89	543	473.2	0.51 ± 0.008	$16.3^{+14.8}_{-3.9}$	$1.97^{+0.38}_{-0.32}$	$0.48^{+0.19}_{-0.27}$	$0.68^{+0.09}_{-0.05}$	$12.7^{+2.0}_{-2.0}$	$1.290^{+0.135}_{-0.079}$	$0.890^{+0.142}_{-0.083}$	$2.270^{+0.045}_{-0.027}$	0.70(124)
84	4639010157	59736.02	2871	461.8	0.50 ± 0.006	$18.6^{+13.0}_{-3.4}$	$1.95^{+0.19}_{-0.22}$	$0.38^{+0.12}_{-0.19}$	$0.73^{+0.07}_{-0.04}$	$11.1^{+1.0}_{-1.4}$	$1.309^{+0.101}_{-0.057}$	$0.823^{+0.104}_{-0.058}$	$2.222^{+0.023}_{-0.013}$	0.75(141)
85	4639010158	59737.09	3290	437.7	0.51 ± 0.004	$17.4^{+6.9}_{-2.8}$	$2.05^{+0.20}_{-0.21}$	$0.38^{+0.10}_{-0.14}$	$0.72^{+0.05}_{-0.03}$	$11.2^{+0.9}_{-1.0}$	$1.239^{+0.059}_{-0.044}$	$0.786^{+0.064}_{-0.047}$	$2.115^{+0.025}_{-0.017}$	0.88(143)
86	4639010159	59738.52	5003	451.8	0.51 ± 0.005	$16.5^{+3.0}_{-2.1}$	$1.98^{+0.15}_{-0.13}$	$0.53^{+0.11}_{-0.11}$	$0.67^{+0.04}_{-0.04}$	$12.5^{+1.3}_{-1.0}$	$1.179^{+0.051}_{-0.044}$	$0.943^{+0.055}_{-0.047}$	$2.212^{+0.019}_{-0.016}$	0.88(147)
87	4639010161	59740.59	2486	418.8	0.51 ± 0.006	$18.0^{+6.6}_{-3.4}$	$2.01^{+0.23}_{-0.19}$	$0.35^{+0.11}_{-0.12}$	$0.70^{+0.04}_{-0.03}$	$11.5^{+1.0}_{-1.0}$	$1.175^{+0.054}_{-0.040}$	$0.731^{+0.060}_{-0.044}$	$1.996^{+0.025}_{-0.017}$	0.70(140)
88	4639010162	59741.50	2384	416.7	0.51 ± 0.005	$16.1^{+4.6}_{-2.7}$	$2.09^{+0.25}_{-0.21}$	$0.42^{+0.11}_{-0.12}$	$0.68^{+0.04}_{-0.03}$	$12.0^{+1.1}_{-1.0}$	$1.137^{+0.052}_{-0.034}$	$0.764^{+0.058}_{-0.039}$	$1.991^{+0.026}_{-0.020}$	0.74(140)
89	4639010164	59743.35	1795	497.3	0.51 ± 0.006	$22.1^{+4.8}_{-4.8}$	$1.81^{+0.16}_{-0.21}$	$0.37^{+0.16}_{-0.22}$	$0.75^{+0.13}_{-0.05}$	$10.9^{+1.4}_{-2.1}$	$1.425^{+0.208}_{-0.096}$	$0.974^{+0.209}_{-0.097}$	$2.489^{+0.020}_{-0.013}$	0.76(139)
90	4639010165	59745.49	1759	467.5	0.52 ± 0.007	$8.5^{+1.9}_{-1.8}$	$4.33^{+1.82}_{-0.97}$	$1.00^{+0.12}_{-0.12}$	$0.58^{+0.06}_{-0.03}$	$14.5^{+1.3}_{-1.9}$	$0.846^{+0.051}_{-0.026}$	$1.429^{+0.145}_{-0.094}$	$2.364^{+0.135}_{-0.090}$	0.70(136)
91	4639010167	59748.06	3385	432.3	0.50 ± 0.006	$24.5^{+16.2}_{-7.0}$	$1.74^{+0.20}_{-0.12}$	$0.28^{+0.17}_{-0.12}$	$0.74^{+0.05}_{-0.06}$	$10.6^{+1.5}_{-1.0}$	$1.219^{+0.092}_{-0.055}$	$0.752^{+0.093}_{-0.056}$	$2.061^{+0.016}_{-0.011}$	0.64(143)
92	4639010168	59749.09	1933	452.4	0.51 ± 0.007	$15.1^{+3.3}_{-2.1}$	$2.07^{+0.21}_{-0.18}$	$0.63^{+0.14}_{-0.15}$	$0.67^{+0.05}_{-0.05}$	$12.6^{+1.8}_{-1.3}$	$1.151^{+0.066}_{-0.058}$	$1.023^{+0.071}_{-0.062}$	$2.265^{+0.028}_{-0.023}$	0.63(138)
93	4639010169	59750.06	677	439.4	0.51 ± 0.010	$11.1^{+2.6}_{-2.5}$	$2.66^{+0.87}_{-0.43}$	$0.80^{+0.20}_{-0.16}$	$0.60^{+0.05}_{-0.07}$	$15.0^{+3.8}_{-1.8}$	$1.057^{+0.062}_{-0.070}$	$1.082^{+0.097}_{-0.088}$	$2.229^{+0.075}_{-0.053}$	0.82(127)
94	4639010170	59751.22	4721	380.8	0.50 ± 0.006	$17.9^{+4.2}_{-2.9}$	$2.04^{+0.20}_{-0.16}$	$0.35^{+0.08}_{-0.08}$	$0.67^{+0.03}_{-0.03}$	$11.7^{+0.9}_{-0.8}$	$1.040^{+0.002}_{-0.002}$	$0.665^{+0.004}_{-0.004}$	$1.795^{+0.003}_{-0.003}$	0.81(144)
95	4639010171	59752.45	1351	391.0	0.50 ± 0.008	$15.8^{+7.5}_{-3.6}$	$2.16^{+0.20}_{-0.30}$	$0.42^{+0.14}_{-0.17}$	$0.69^{+0.03}_{-0.04}$	$11.2^{+1.3}_{-1.2}$	$1.059^{+0.003}_{-0.003}$	$0.715^{+0.005}_{-0.005}$	$1.864^{+0.004}_{-0.004}$	1.00(134)
96	4639010172	59753.68	3837	376.9	0.50 ± 0.006	$20.1^{+8.9}_{-3.9}$	$1.97^{+0.20}_{-0.17}$	$0.31^{+0.10}_{-0.11}$	$0.72^{+0.04}_{-0.03}$	$10.4^{+0.9}_{-0.9}$	$1.062^{+0.002}_{-0.002}$	$0.651^{+0.004}_{-0.004}$	$1.803^{+0.003}_{-0.003}$	0.72(142)
97	4639010173	59754.40	4201	371.4	0.51 ± 0.005	$15.6^{+2.6}_{-2.0}$	$2.09^{+0.19}_{-0.15}$	$0.50^{+0.09}_{-0.09}$	$0.65^{+0.03}_{-0.03}$	$12.0^{+1.1}_{-0.9}$	$0.961^{+0.002}_{-0.002}$	$0.742^{+0.004}_{-0.004}$	$1.794^{+0.003}_{-0.003}$	0.68(143)
98	4639010174	59755.44	507	377.5	0.50 ± 0.008	$23.9^{+2.8}_{-8.3}$	$1.65^{+0.20}_{-0.19}$	$0.38^{+0.19}_{-0.25}$	$0.67^{+0.11}_{-0.06}$	$11.7^{+2.3}_{-2.5}$	$0.986^{+0.003}_{-0.003}$	$0.760^{+0.007}_{-0.007}$	$1.836^{+0.006}_{-0.006}$	0.72(120)
99	4639010176	59757.50	1513	301.1	0.51 ± 0.009	$12.4^{+2.8}_{-2.4}$	$2.56^{+0.61}_{-0.37}$	$0.55^{+0.10}_{-0.11}$	$0.60^{+0.03}_{-0.03}$	$12.7^{+1.4}_{-1.1}$	$0.749^{+0.002}_{-0.002}$	$0.630^{+0.004}_{-0.004}$	$1.469^{+0.004}_{-0.004}$	0.75(131)
100	4639010177	59760.00	3048	273.4	0.50 ± 0.007	$19.0^{+5.2}_{-3.1}$	$1.91^{+0.19}_{-0.16}$	$0.34^{+0.08}_{-0.09}$	$0.63^{+0.03}_{-0.03}$	$11.1^{+1.0}_{-0.9}$	$0.699^{+0.002}_{-0.002}$	$0.476^{+0.003}_{-0.003}$	$1.265^{+0.003}_{-0.003}$	0.88(138)
101	4639010178	59761.03	3847	265.2	0.50 ± 0.005	$18.4^{+3.6}_{-2.5}$	$1.92^{+0.15}_{-0.13}$	$0.36^{+0.07}_{-0.07}$	$0.61^{+0.03}_{-0.02}$	$11.6^{+0.9}_{-0.8}$	$0.671^{+0.002}_{-0.002}$	$0.465^{+0.003}_{-0.003}$	$1.226^{+0.003}_{-0.003}$	0.84(140)
102	4639010180	59763.03	1819	283.6	0.51 ± 0.007	$24.3^{+18.4}_{-5.4}$	$1.72^{+0.17}_{-0.15}$	$0.29^{+0.11}_{-0.13}$	$0.66^{+0.03}_{-0.04}$	$10.3^{+1.2}_{-1.2}$	$0.740^{+0.002}_{-0.002}$	$0.499^{+0.004}_{-0.004}$	$1.329^{+0.003}_{-0.003}$	0.80(134)
103	4639010181	59764.00	3600	254.2	0.50 ± 0.006	$11.9^{+2.1}_{-2.0}$	$2.87^{+0.63}_{-0.39}$	$0.53^{+0.07}_{-0.07}$	$0.58^{+0.02}_{-0.02}$	$12.0^{+1.0}_{-0.8}$	$0.612^{+0.002}_{-0.002}$	$0.568^{+0.003}_{-0.003}$	$1.270^{+0.003}_{-0.003}$	0.89(139)
104	4639010182	59765.16	1409	235.9	0.51 ± 0.009	$16.9^{+4.0}_{-2.8}$	$1.99^{+0.27}_{-0.20}$	$0.39^{+0.08}_{-0.09}$	$0.56^{+0.03}_{-0.03}$	$12.7^{+1.3}_{-1.1}$	$0.578^{+0.002}_{-0.002}$	$0.426^{+0.003}_{-0.003}$	$1.094^{+0.003}_{-0.003}$	0.82(127)
105	4639010184	59767.22	972	177.4	0.47 ± 0.010	$19.2^{+5.5}_{-3.7}$	$1.91^{+0.28}_{-0.20}$	$0.29^{+0.07}_{-0.07}$	$0.52^{+0.03}_{-0.03}$	$12.5^{+1.4}_{-1.1}$	$0.406^{+0.002}_{-0.002}$	$0.287^{+0.003}_{-0.003}$	$0.782^{+0.003}_{-0.003}$	0.92(118)

Table 3:: The results of the spectral fit of the NICER spectra in the 0.4–10 keV range with
tbabs*thcomp*(bb+diskbb)

No	obsid	Time MJD	Exposure s	Rate cts/s	N_{H} 10^{22} cm^{-2}	τ	kT_{e} keV	f_{sc}	kT_{disk} keV	R_{disk} km	F_{disk} 10^{-9}	F_{corona} 10^{-9}	F_{total} 10^{-9}	χ^2_{ν} (d.o.f.)
106	4639010185	59768.02	2603	88.6	0.45 ± 0.021	$18.5^{+2.3}_{-2.5}$	$2.46^{+0.52}_{-0.29}$	$0.35^{+0.04}_{-0.04}$	$0.29^{+0.02}_{-0.02}$	$24.3^{+5.9}_{-3.8}$	$0.138^{+0.001}_{-0.001}$	$0.266^{+0.002}_{-0.002}$	$0.495^{+0.002}_{-0.002}$	0.89(99)
107	4639010186	59769.44	2875	62.5	0.43 ± 0.025	$16.9^{+3.0}_{-2.0}$	$2.22^{+0.26}_{-0.23}$	$0.60^{+0.08}_{-0.12}$	$0.26^{+0.05}_{-0.04}$	$19.2^{+9.9}_{-5.4}$	$0.053^{+0.001}_{-0.001}$	$0.186^{+0.001}_{-0.001}$	$0.329^{+0.001}_{-0.001}$	0.88(124)
108	4639010187	59773.69	1057	56.0	0.53 ± 0.007	$10.6^{+1.3}_{-1.2}$	$3.49^{+0.58}_{-0.43}$	$0.85^{+0.06}_{-0.03}$	$0.09^{+0.01}_{-0.01}$	$140.4^{+0.9}_{-0.9}$	$0.043^{+0.001}_{-0.001}$	$0.234^{+0.002}_{-0.002}$	$0.367^{+0.002}_{-0.002}$	1.26(110)
109	4639010188	59774.34	1450	55.1	0.50 ± 0.006	$12.6^{+1.1}_{-0.9}$	$2.77^{+0.24}_{-0.21}$	$0.81^{+0.05}_{-0.06}$	$0.08^{+0.01}_{-0.01}$	$176.0^{+1.1}_{-1.1}$	$0.037^{+0.001}_{-0.001}$	$0.207^{+0.001}_{-0.001}$	$0.334^{+0.001}_{-0.001}$	1.08(115)
110	4639010189	59781.70	2810	60.5	0.54 ± 0.006	$6.7^{+1.5}_{-2.2}$	$8.05^{+6.77}_{-2.16}$	$0.85^{+0.06}_{-0.04}$	$0.10^{+0.01}_{-0.01}$	$132.9^{+0.5}_{-0.5}$	$0.053^{+0.001}_{-0.001}$	$0.389^{+0.002}_{-0.002}$	$0.532^{+0.002}_{-0.002}$	0.79(125)
111	4639010190	59782.02	5429	59.9	0.53 ± 0.005	$7.1^{+1.1}_{-1.6}$	$7.20^{+3.29}_{-1.77}$	$0.86^{+0.04}_{-0.03}$	$0.10^{+0.01}_{-0.01}$	$129.5^{+0.4}_{-0.4}$	$0.051^{+0.001}_{-0.001}$	$0.361^{+0.001}_{-0.001}$	$0.502^{+0.001}_{-0.001}$	0.79(133)
112	4639010191	59783.05	6267	60.0	0.52 ± 0.005	$7.1^{+1.3}_{-2.2}$	$8.51^{+6.50}_{-1.99}$	$0.74^{+0.04}_{-0.02}$	$0.11^{+0.01}_{-0.01}$	$122.7^{+0.3}_{-0.3}$	$0.053^{+0.001}_{-0.001}$	$0.438^{+0.001}_{-0.001}$	$0.581^{+0.001}_{-0.001}$	0.96(135)
113	4639010192	59784.02	3321	57.6	0.54 ± 0.005	$9.7^{+1.2}_{-1.2}$	$4.33^{+0.89}_{-0.62}$	$0.81^{+0.04}_{-0.04}$	$0.09^{+0.01}_{-0.01}$	$149.5^{+0.6}_{-0.6}$	$0.047^{+0.001}_{-0.001}$	$0.278^{+0.001}_{-0.001}$	$0.415^{+0.001}_{-0.001}$	0.78(125)
114	4639010193	59785.18	479	53.7	0.57 ± 0.009	$7.6^{+1.2}_{-1.5}$	$4.45^{+1.93}_{-0.96}$	$0.98^{+0.01}_{-0.08}$	$0.09^{+0.01}_{-0.01}$	$168.4^{+1.8}_{-1.8}$	$0.041^{+0.001}_{-0.001}$	$0.194^{+0.003}_{-0.003}$	$0.325^{+0.002}_{-0.002}$	0.94(99)
115	4639010194	59786.35	657	48.5	0.57 ± 0.008	$4.5^{+2.2}_{-2.6}$	$12.05^{+35.92}_{-5.34}$	$0.87^{+0.01}_{-0.08}$	$0.10^{+0.01}_{-0.01}$	$115.0^{+1.1}_{-1.0}$	$0.038^{+0.001}_{-0.001}$	$0.279^{+0.003}_{-0.003}$	$0.407^{+0.003}_{-0.003}$	1.08(94)
116	4639010195	59787.18	570	47.8	0.54 ± 0.008	$10.9^{+1.6}_{-1.4}$	$3.18^{+0.62}_{-0.43}$	$0.80^{+0.07}_{-0.07}$	$0.10^{+0.01}_{-0.01}$	$103.6^{+1.2}_{-1.2}$	$0.029^{+0.001}_{-0.001}$	$0.170^{+0.002}_{-0.002}$	$0.289^{+0.002}_{-0.002}$	0.88(92)
117	4639010196	59791.24	213	43.6	0.48 ± 0.009	$2.9^{+3.5}_{-1.5}$	$24.62^{+62.09}_{-12.47}$	$0.90^{+0.01}_{-0.14}$	$0.06^{+0.01}_{-0.01}$	$244.4^{+5.9}_{-5.9}$	$0.019^{+0.001}_{-0.001}$	$0.268^{+0.004}_{-0.004}$	$0.377^{+0.004}_{-0.004}$	1.14(72)

a : The model parameters: the optical depth τ , the electron temperature kT_{e} , the cover factor f_{sc} , the accretion disk temperature kT_{disk} and the inner disk radius R_{diskbb} at a distance of 7.56 kpc and in the face-on scenario (inclination angel $\theta=0$), the bolometric flux of the diskbb F_{diskbb} , the bolometric flux of the corona F_{diskbb} , and the total bolometric flux F_{total} are in units of $10^{-9} \text{ erg/cm}^2/\text{s}$, reduced χ^2_{ν} and the degree of freedom (d.o.f.).

b : Please note that the 'propeller effect' time is between **obsids 4639010184 and 4639010185**.

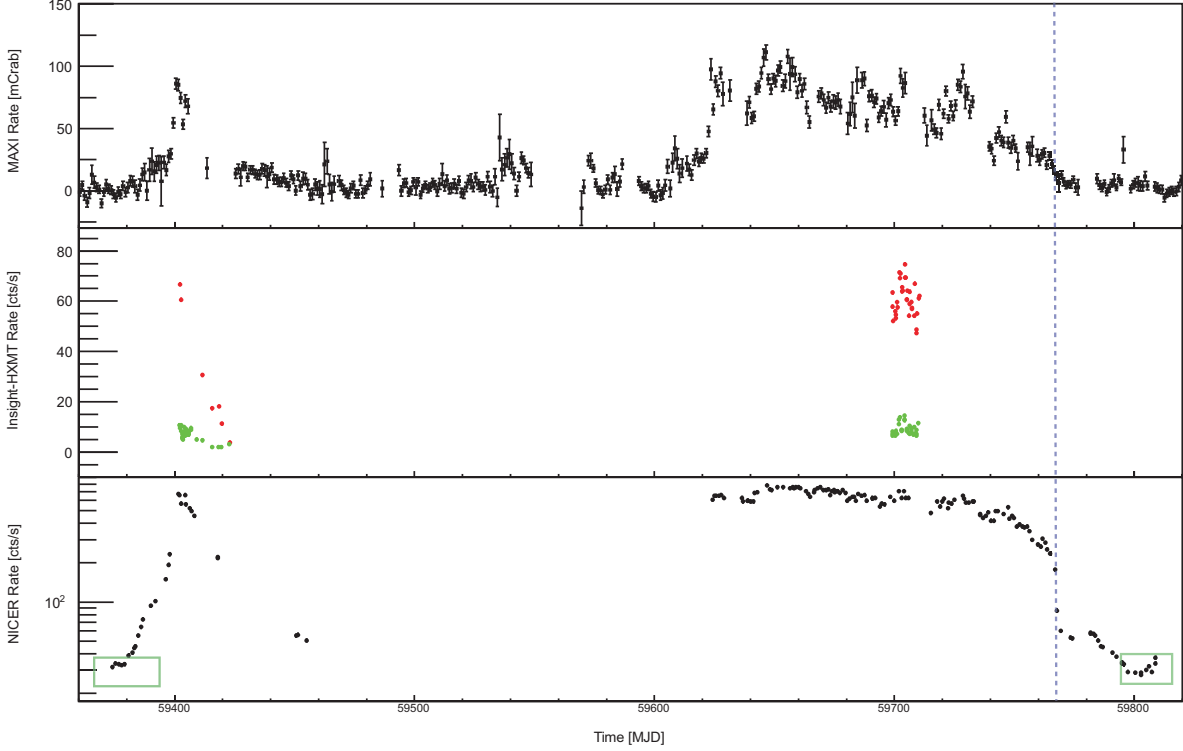


Fig. 1.— Top panel: daily light curves of 4U 1730–22 by MAXI (black, 2–20 keV) during the outburst in 2021 and 2022. Middel panel: Net light curves of 4U 1730–22 by LE (1–10 keV, red) and ME (8–30 keV, green) which are rebinned by one obsid (~ 10000 s). Bottom panel: Net light curves of 4U 1730–22 by NICER (0.3–12 keV, its full energy band) which are rebinned by one obsid (~ 3000 s). Please note the error bars of the light curves of LE, ME, and NICER are smaller than the size of the symbols; and the NICER lightcurves are plotted in a diagram of log count rate versus time. The ‘propeller effect’ time is marked by a blue line. **The data points in the green box indicate the obsids with count rate < 40 cts/s at the onset of the outburst in 2021 and the extinction of the outburst in 2022, which are stacked and fitted respectively; the derived model parameters from the two stacked spectra are shown in Table 1.**

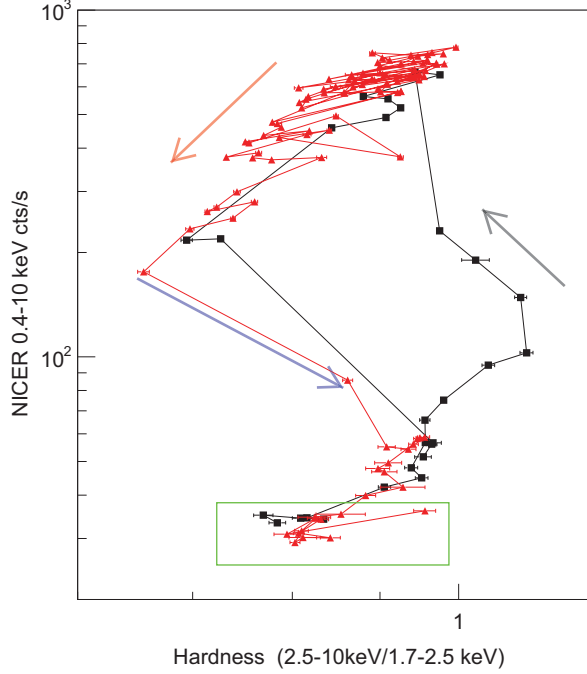


Fig. 2.— Hardness-intensity diagram for NICER observations. Hardness is defined as the NICER count-rate ratio in the $(2.5\text{--}10\text{ keV})/(1.7\text{--}2.5\text{ keV})$ bands, intensity is defined as the count rate of NICER in $0.4\text{--}10\text{ keV}$. Each point in the diagram represents one obsid with an exposure time of $\sim 1000\text{--}5000\text{ s}$. The black points and red points represent the outburst in 2021 and 2022, respectively. For the outburst in 2021, it began at the bottom left and evolved in an anticlockwise loop, **as shown in the gray arrow**. For the outburst in 2022, the NICER observations missed the outburst’s onset and the first observation is located at the top right and evolved in an anticlockwise direction, ending at the bottom left, **as shown in the red arrow**. The ‘propeller effect’ time is marked by a blue arrow. **The black and red points in the green box indicate the onset of the outburst in 2021 and the extinction of the outburst in 2022, which are $< 40\text{ cts/s}$ and stacked and fitted respectively.**

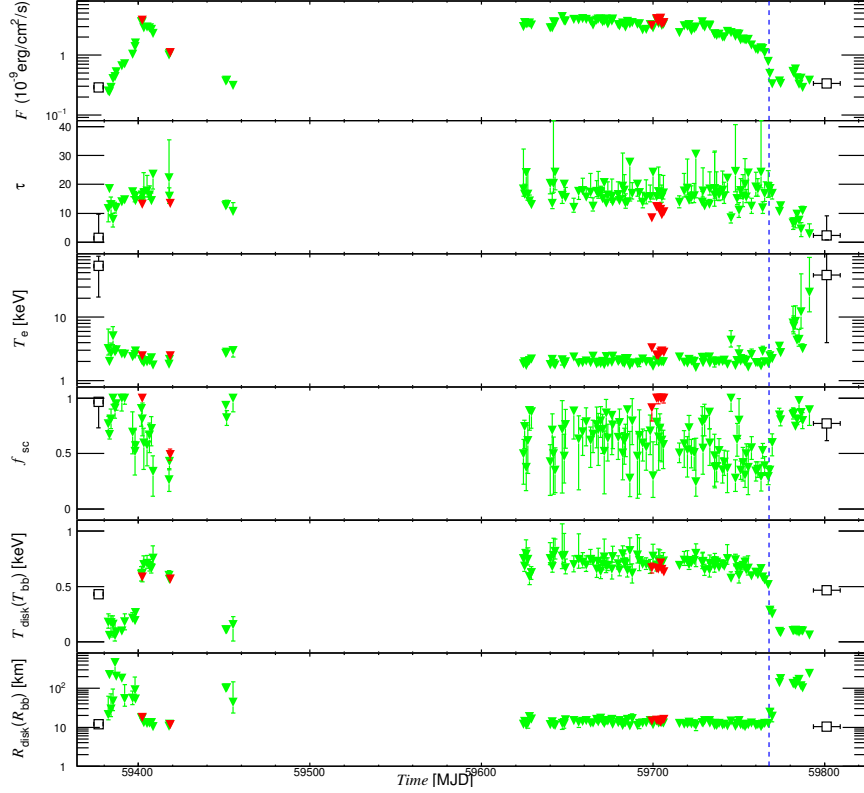


Fig. 3.— Time evolution of best-fitting parameters for the best-fitting model $\text{tbabs}^*\text{thcomp}^*\text{bbody}$ (black) and $\text{tbabs}^*\text{thcomp}^*(\text{bbody}+\text{diskbb})$ (red and green) from 4U 1730–22 during its 2021 and 2022 outbursts, including the bolometric flux F , the optical depth τ , the electron temperature T_e , the cover factor f_{sc} , the accretion disk/blackbody temperature $kT_{\text{disk}}/kT_{\text{bb}}$ and the inner disk radius/blackbody radius $R_{\text{diskb}}/R_{\text{bb}}$ at a distance of 7.56 kpc and in the face-on scenario (inclination angel $\theta=0$). The black markers represent the parameters derived from $\text{tbabs}^*\text{thcomp}^*\text{bbody}$ in the onset and extinction time of the outbursts observed by NICER. The green and red indicate the parameters derived from $\text{tbabs}^*\text{thcomp}^*(\text{bbody}+\text{diskbb})$ (with **fixed blackbody parameters derived from the aforementioned spectral fitting of the onset of the outburst**) observed by NICER and the joint observations of NICER and Insight-HXMT, respectively. The ‘propeller effect’ time is marked by a blue line.

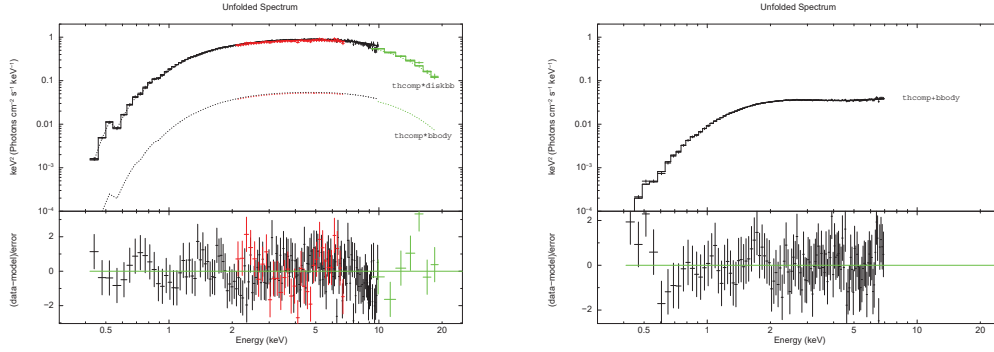


Fig. 4.— Left panel: the results of the spectral fits with data from NICER (black), LE (red), and ME (green) at the peak flux of the outburst in 2021 by $\text{cons}*\text{tbabs}*\text{thcomp}*(\text{bb}+\text{diskbb})$ with fixed blackbody parameters derived from the spectral fitting results of the onset of the outburst. Right panel: the results of the spectral fits with NICER data at the end of the outburst in 2022 by $\text{tbabs}*\text{thcomp}*\text{bb}$.

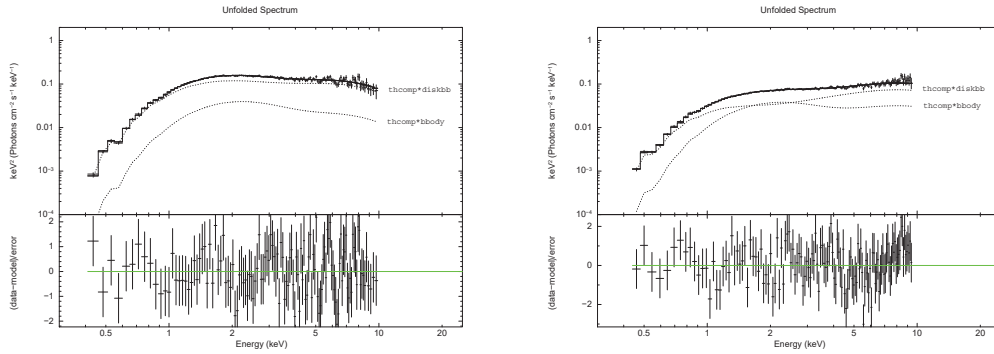


Fig. 5.— The results of the spectral fits of the obsid 4639010184 (left) and obsid 4639010185 (right), i.e., the two obsids at the transition time when the ‘propeller effect’ occurred at the decay phase of the outburst in 2022 by $\text{tbabs}*\text{thcomp}*(\text{bb}+\text{diskbb})$.

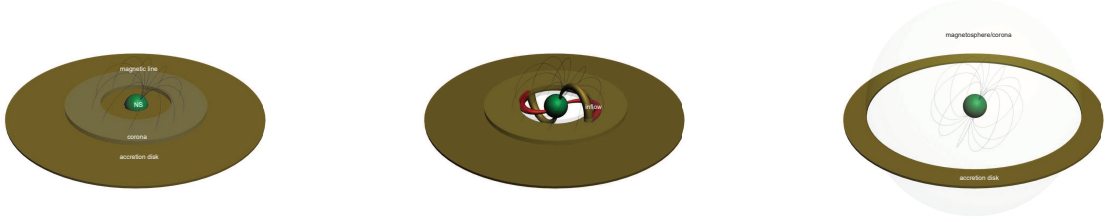


Fig. 6.— Illustration of the central region of an NS LMXB in the high/soft state (left, before the propeller effect), just after the propeller effect (middle) and the tail of the outburst (right). Before the propeller effect, the accretion disk extends to the NS surface; and just after that the accretion disk is truncated near the corotation radius, and partial material leaks to the NS surface; at the end of the outburst, there is a scenario of the magnetospheric accretion and the spherical corona.